Investigation of Chip Production Rate as an Indicator of Micromilling Tool Wear

by

Anuj Kishorkumar Bajaj

A Thesis Presented in Partial Fulfillment
of the Requirements of the Degree
Master of Science

Approved November 2015 by the
Graduate Supervisory committee:

Angela Sodemann, Chair
Jennifer Bekki
Keng Hsu

ARIZONA STATE UNIVERSITY

December 2015

ABSTRACT

The demand for miniaturized components with feature sizes as small as tens of microns and tolerances as small as 0.1 microns is on the rise in the fields of aerospace, electronics, optics and biomedical engineering. Micromilling has proven to be a process capable of generating the required accuracy for these features and is an alternative to various non-mechanical micro-manufacturing processes which are limited in terms of cost and productivity, especially at the micro-meso scale. The micromilling process is on the surface, a miniaturized version of conventional milling, hence inheriting its benefits. However, the reduction in scale by a few magnitudes makes the process peculiar and unique; and the macro-scale theories have failed to successfully explain the micromilling process and its machining parameters. One such characteristic is the unpredictable nature of tool wear and breakage. There is a large cost benefit that can be realized by improving tool life. Workpiece rejection can also be reduced by successfully monitoring the condition of the tool to avoid issues. Many researchers have developed Tool Condition Monitoring and Tool Wear Modeling systems to address the issue of tool wear, and to obtain new knowledge. In this research, a tool wear modeling effort is undertaken with a new approach. A new tool wear signature is used for real-time data collection and modeling of tool wear. A theoretical correlation between the number of metal chips produced during machining and the condition of the tool is introduced. Experimentally, it is found that the number of chips produced drops with respect to the feedrate of the cutting process i.e. when the uncut chip thickness is below the theoretical minimum chip thickness.

DEDICATION

To my family & friends

To the community of science and engineering

ACKNOWLEDGMENTS

I wish to express my sincere thanks to Drs. Jennifer Bekki and Keng Hsu, to contribute time and efforts for the success of this thesis. I would like to express my gratitude to Dr. Angela Sodemann, for being an excellent mentor and providing me support and guidance while always showing me the path for success. Without her efforts, time and energy, this thesis would not be possible.

I would like to thank my colleagues on Dr. Sodemann's research team and capstone members for their contributions and support towards the project, which helped achieve the success of the project.

I am grateful to all my friends for their constant encouragement and omnipresence which has made my work enjoyable.

Finally, I would like to thank my family: My father, mother and my sister for inspiring me to achieve what I perceived was impossible. They continue to support me to achieve my life goals.

TABLE OF CONTENTS

Page

CHAPTER Page

LIST OF TABLES

Table Page

LIST OF FIGURES

Figure Page

Figure Page

1 INTRODUCTION

Small metallic parts with feature sizes less than 1mm and tolerances as small as 0.1 micron are in demand across many industries such as the biomedical, defense, electronics, optical technologies and aerospace industries. Many micro-manufacturing processes have been developed to meet the demand and the benefits of miniaturization. Non-mechanical processes include micro-electro discharge machining (EDM), laser-cutting, micro-etching, electron beam machining, while mechanical micro-manufacturing include micro-turning and micromilling. Micromilling has been used to develop biomedical devices such as micro-scale piercings for implants on living tissue [1]. Micromilling is also used in the fabrication of micro-acoustic lenses for ultrasound transducers [2]. Processes such as X-ray lithography and micromilling are used for the fabrication of Bio-mems devices [3]. Figure 1 shows the broad classification of the micro-manufacturing processes.

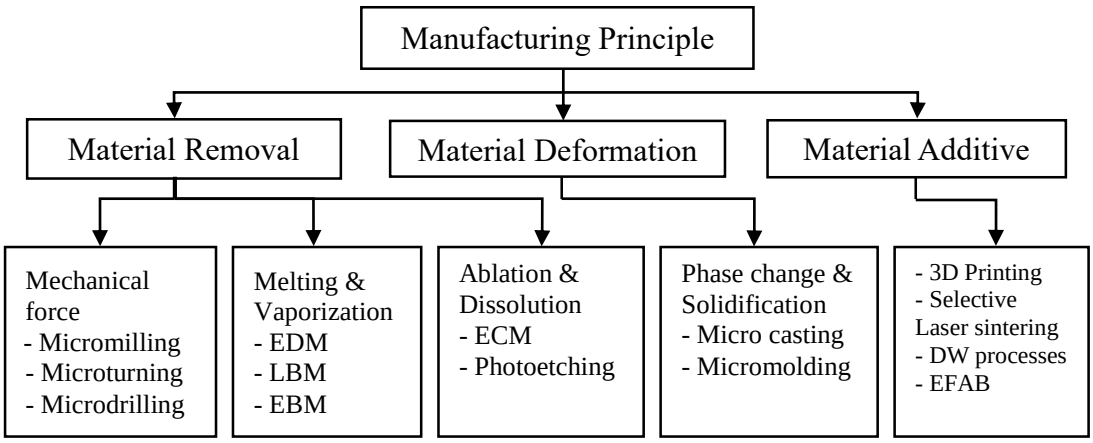

Figure 1: Classification of micro-manufacturing operations

Among the various micro-manufacturing processes, the non-mechanical processes are limited by various constraints. There is a fundamental limitation on the machinability of certain materials based on their chemical and electrical properties.

Processes such as micro-EDM and micro-ECM have very low material removal rates in comparison to the mechanical micro-machining processes [4]. Although mechanical micro-machining processes do not have the minimum unit removal capability of the non-mechanical processes, they are capable of higher machining speeds, are comparatively low cost and provide high flexibility and little restriction on material machinability. Mechanical micro-machining processes are capable of meeting the accuracy and tolerance requirements at the micro-meso scale, with workpiece sizes above 500μm [5]. Sandia Laboratories [6], believe that the requirement to fill the gap between the nano/micro-scale and the macro-scale is becoming increasingly important, a space which mechanical micro-machining can economically fill.

Micromilling has been developed as a scaled-down version of the conventional milling process. Microturning and micro-drilling have fewer applications and capabilities as compared to micromilling. Micromilling has the ability to generate features on planar surfaces as well as contoured workpieces. It is cost effective and is widely used due to its mass production capabilities [5], [7].

In this Chapter, section 1.1 describes the problem statement for the research. Section 1.2 explores literature regarding micromilling tool wear modeling systems and measurement approaches. Sections 1.3 and 1.4 outline the research objectives and the hypothesis for this thesis.

1.1 PROBLEM STATEMENT

The process of micromilling is relatively new and has not been extensively researched as compared to the conventional macro-scale milling. Many aspects of micromilling require extensive research in order to better understand the process and

improve its productivity. Some of the research areas are micro-tool development, precision machine tool development, chip formation process, tool materials and metrology and tool wear and breakage.

The process of micromilling uses micro end mills as the cutting tools, which are relatively expensive due to the precision manufacturing processes required to produce them. Thus, the cost of the cutting tool increases with decreasing tool size. In some cases, the cutting tools require special treatment in order to machine abrasive or extremely hard metals, such as diamond coatings, making the tools extremely costly. A commercially available tungsten-carbide micro-end mill of 200 μm diameter currently can cost $30 USD per tool. The cost of the process also increases due to the need of a precision machine tool to meet the accuracy and tolerance requirement of the parts that would be machined.

Micro end mills have a diameter of 1mm and can be as small as 50μm. Therefore, the spindle speed required is very high, in order to achieve the necessary cutting speed and develop enough cutting force. The process also requires high feedrates to successfully produce a cut [8]. The tools are small and have significantly lower strength compared to a macro-size tool; this makes tool wear and breakage a very severe problem. Thus, tool wear in micromilling is an important area of research. Chae et al. [5] suggest that tool wear and breakage caused by the inherently high cutting forces and small tool size, is a major challenge in micromilling.

This problem of tool wear and breakage is aggravated as tool life is extremely short and unpredictable. These tools cannot be re-sharpened and do not have the possibility of using cutting inserts, making them single-time use tools. Machining with a worn tool leads to poor workpiece surface finish and dimensional accuracy. There is

a large cost benefit that can be availed by monitoring and predicting tool wear to improve tool life and lower rejection of workpieces. These factors have made tool wear a crucial area of interest and research. The pursuit of this research area has led to development of Tool Condition Monitoring (TCM) and Tool Wear Modeling (TWM) systems for understanding, monitoring, predicting, and improving tool condition during machining [7], [8].

1.2 MICROMILLING TOOL WEAR MODELING

Based on the objective of the tool wear research, the system developed by a researcher is either a TCM system or a TWM system. TCM systems aim mainly to accurately predict the condition of the tool during machining, based upon a tool wear model either provided a-priori or obtained through a machine learning process. These systems inherently need to work 'online' which means that the data collection and analysis take place in real-time, during the cutting process. The input into the system is an 'indirect' measurement on the tool, such as cutting force or acoustic emissions, and the output is the predicted or estimated state of wear of the tool. These systems can then be used to implement adaptive control and reduce accuracy errors to improve productivity. This information is also used to predict and classify the state of the tool as new, used or worn. Many systems of this type have been researched, and are discussed here in Chapter 2.

The aim of TWM systems is to generate or develop a model of tool wear. Some modeling efforts are done by computer simulation along with, or followed by experimentation. The data that is obtained is used to understand the impact of the cutting process parameters such as spindle speed, feedrate, or depth of cut on the tool life and wear. The input to a TWM system is a 'direct' measure of the tool, such as the

measurement of the tool under a microscope, and the output is a tool cutting model as a function of cutting parameters. The measurements performed on the tools and workpieces are often done using expensive equipment such as scanning electron microscope, which are not readily accessible. Table 1 shows a breakdown of TWM and TCM systems, their purpose and their features.

Table 1: Breakdown of Tool wear research systems

	Online System	**Offline System**
Tool Condition Monitoring	• Used for monitoring • Use 'indirect' signatures and complex algorithms	N/A
Tool Wear Modeling	Area of research of this work	• Have predictive capability • Use 'direct' methods and expensive equipment

1.3 RESEARCH OBJECTIVES

The macro-scale mechanical machining processes have been widely studied. These processes also have established equations, process constants and experimental data to determine optimum machining parameters and tool life. This data is summarized in the widely-used Machinery's Handbook [9]. However, it is widely recognized that the information from the Machinery's Handbook does not apply at the microscale; for example, recommendations from the Machinery's Handbook would recommend a spindle speed of about 1,000,000 rpm for cutting Al 6061 with a 100 micron-diameter micro end mill. Accurate knowledge of feeds and speeds is currently not available for micromilling. On the other hand, information obtained from tool wear modeling is used to evaluate and develop tool wear models which can establish fundamental governing mechanics of the process, and parameters used during machining.

The experiments that are performed on offline TWM are extremely tedious. To obtain enough data, one must repeatedly pause machining to observe the tool condition and workpiece under a microscope. Chae et al. [5], recommended that "Developing new inspection and testing techniques will have a significant impact". An online tool wear modeling system would eliminate the need for expensive tool inspection equipment and would be able to obtain data in real-time and very efficiently. This thesis proposes the indirect tool wear signature of chip production rate as a means to create an online tool wear modeling system. To this end, this thesis aims at achieving three main objectives:

- Objective 1: To develop a prototype Online Tool Wear Modeling system that utilizes chip production rate as an indirect signature.
- Objective 2: To evaluate the effectiveness of the prototype device to measure chip production rate.
- Objective 3: To provide an empirical proof-of-concept for chip production rate as an indirect signature of tool wear.

1.4 HYPOTHESIS

In micromilling, the reduction in scale by several magnitudes has resulted in and amplified various effects, which are not observed, or are not dominant in the conventional macro-scale. These are broadly termed as 'scale-effects'. These effects are explained in Chapter 2 in detail. The concept of a minimum uncut chip thickness (MCT) is one such scale-effect, and has been considered a critical parameter for metal cutting in micromilling. The significance of this parameter is that below the MCT threshold, metal cutting does not take place. In other words, chip formation does not occur when the cutting tooth of the tool passes over the workpiece when in violation of

the threshold. To stay above this MCT, there has to be enough thickness of uncut metal when one cutting tooth starts cutting. This is achieved by keeping a sufficiently high feedrate.

The MCT of a tool depends on another tool geometry parameter which is its cutting edge radius. The MCT value increases with increasing cutting edge radius. The cutting edge radius changes with change in tool condition. It generally tends to increase, making the tool blunt or worn as cutting progresses. Hence, with enough wear of the tool, the feedrate of the cutting process is not sufficient and the MCT threshold is crossed. Theoretically, a sharp, sudden decrease in the chip production rate should be observed at a particular amount of tool wear. This is visually seen in Figure 2, where Kim et al. [10] presented a theoretical graph showing a relation between expected chip formation and feed per tooth. The graph also shows that the effect is dominant in tools with small diameters i.e. micro cutting tools.

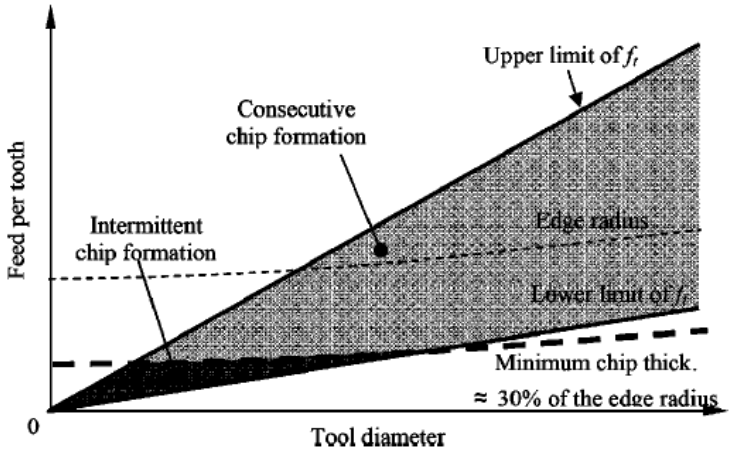

Figure 2: Feed per tooth and Minimum Chip Thickness [10]

The cutting tool that is commonly used for micromilling is a 2-flute micro end mill, which has two cutting teeth. When cutting at a sufficient feedrate, it can be assumed that the operation is taking place above the minimum chip thickness. At this

condition, it is expected that exactly one chip will be produced at each tooth pass. This is illustrated in Figure 3, which shows a simulation performed by Kim et al. [11]. In a condition where the MCT threshold is violated, one cutting tooth will slip and not cut the workpiece, thereby not generating a chip. But, due to a constant velocity in the cutting direction, the second cutting tooth should be above the MCT threshold, and hence will cut the workpiece. In this condition, it can be hypothesized that the chip production rate will be halved.

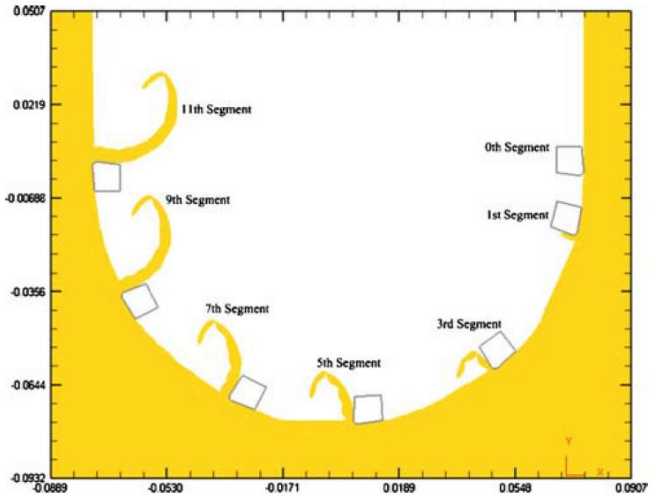

Figure 3: Chip formation analysis in micromilling shown in its various stages [11]

The TWM system developed in this thesis looks to leverage this relationship between cutting edge radius, feedrate, and chip production rate to model tool wear online (without interruption of the cutting process). The hypothesis can be stated as:

During micromilling, if the cutting edge radius of the micro end mill wears so that the uncut chip thickness drops below the minimum chip thickness, the number of chips produced per unit time will drop by approximately half as compared to when the tool is new.

This hypothesis can be tested and will require development of a new online TWM system.

1.5 THESIS OVERVIEW

Chapter 1 touched on the problem of tool wear in micromilling and the various systems used by researchers for monitoring and predicting tool condition. The objectives and the research hypothesis were also stated. In Chapter 2, the background concepts such as micromilling scale effects, minimum chip thickness and its impact on machining parameters are discussed. The use of machine vision in manufacturing is also touched upon. In Chapter 3, the concept, sub-system development and system integration for the Tool Wear Modelling (TWM) system are described. The governing equations for the system are also derived. An image processing algorithm is also described. Chapter 4 defines the variables of the TWM system, the experimental design, and how the experiment results will evaluate the hypothesis. The equipment and procedure used for the experiments are also briefly described. Chapter 5 records the results and the data analysis for all the experiments. Chapter 6 presents the evaluation of the hypothesis and the conclusions to the objectives of the thesis. Chapter 7 outlines future work and opportunities for the research going forward. References and Appendices follow.

2 LITERATURE REVIEW

This Chapter explains the concepts necessary to understand the micromilling process and the stated hypothesis. Section 2.1 touches upon the background concepts such as the differences between the macro-scale and the micro-scale in mechanical machining, the minimum chip thickness effect of micromilling and the use of machine vision systems in manufacturing. Section 2.2 presents the various forms and definitions of tool wear in micro end mills. Section 2.3 outlines the various tool condition monitoring and tool wear modeling efforts pursued by various researchers and the results they obtained.

2.1 BACKGROUND CONCEPTS

2.1.1 Macro vs micro-scale milling

Metal cutting processes at the macro-level have been researched for many years. That has provided the background information and theories of metal cutting. The result of these theories and models was the improvement in tool design, tool life, optimization of machining parameters such as spindle speed, depth of cut and feedrate for various metal-cutting processes. Merchant [12], [13] established a theory for orthogonal cutting. This theory included the derivation of a cutting-force model which made possible the calculation of ground-truth parameters such as the coefficient of friction, shear stain, the work done and so on. Merchant was able to establish force relations and generate a condensed diagram called the ‘Merchant circle’, shown in Figure 4.

Some assumptions were made prior to deriving this theory. It was assumed that the tool has a fully sharp cutting edge, meaning there is no curvature at the cutting tip of the tool; the cutting edge radius is neglected. Such assumptions have proven to work

well in macro-scale machining. However, when the equations derived from these theories are applied to the microscale, the results obtained are unrealistic.

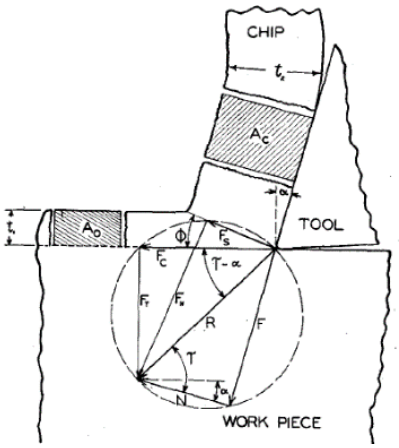

Figure 4: Cutting force diagram at shear plane for macro-milling [12]

Hence, this assumption fails to be valid at the microscale [14], [15]. The tool cutting edge radius in the case of micromachining is comparable to the grain size of the material being machined and sometimes, comparable or even greater than the uncut chip thickness, which is not the case for the macro-scale. Due to this, it is not accurate to neglect the tool cutting edge radius, or assume a positive tool rake angle. Two aspects need to be taken into account due to this:

(1) The clearance face of the cutting tool rubs on the workpiece due to elastic recovery of the workpiece

(2) The rake angle of the tool is effectively negative, hence stresses along the rake face at the interface will be large [16]. This is illustrated in Figure 5.

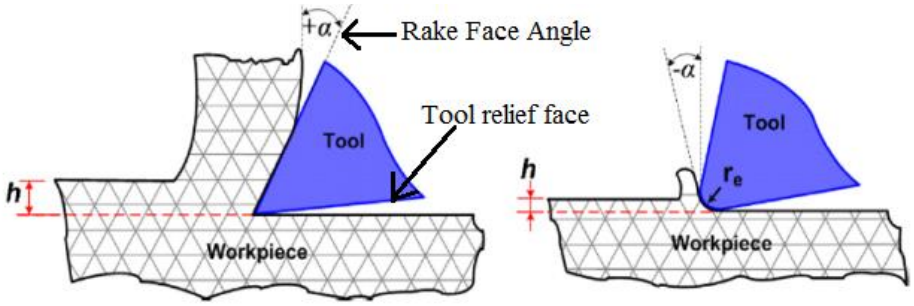

Figure 5: Difference between the macro and micro-scale *(edited for labeling)* [16]

2.1.2 Minimum Chip Thickness effect

The concept of minimum chip thickness was touched upon in Chapter 1. Many researchers have developed cutting models that incorporate the curved nature of the cutting edge, and defined the parameter of minimum chip thickness. Ikawa et al. [17] classified the minimum thickness of cut or minimum chip thickness (MCT) as the most critical parameter in micromachining. Their theory incorporated a round-edged tool and they defined MCT as the critical value of thickness below which no stable chip formation would take place. Aramcharoen and Mativenga [16] have termed this phenomenon as one of the many characteristics of the micro scale referred to as "size-effects". According to them, when Uncut Chip Thickness (UCT) is below the MCT threshold, the tool begins to rub on the surface of the workpiece rather than creating a metal shearing plane. Thus, no cutting takes place and no chip is formed. This 'rubbing' of the tool is generally referred to as 'ploughing'. The workpiece material is compressed and then recovers after the tool passes. This is an 'elastic recovery' of the workpiece material. Only with UCT larger than MCT, chip formation is possible.

Figure 6 shows the effect of uncut chip thickness on chip formation at the microscale. It shows chip formation and material removal in the case of a large uncut chip thickness and shows elastic recovery for the case of low uncut chip thickness.

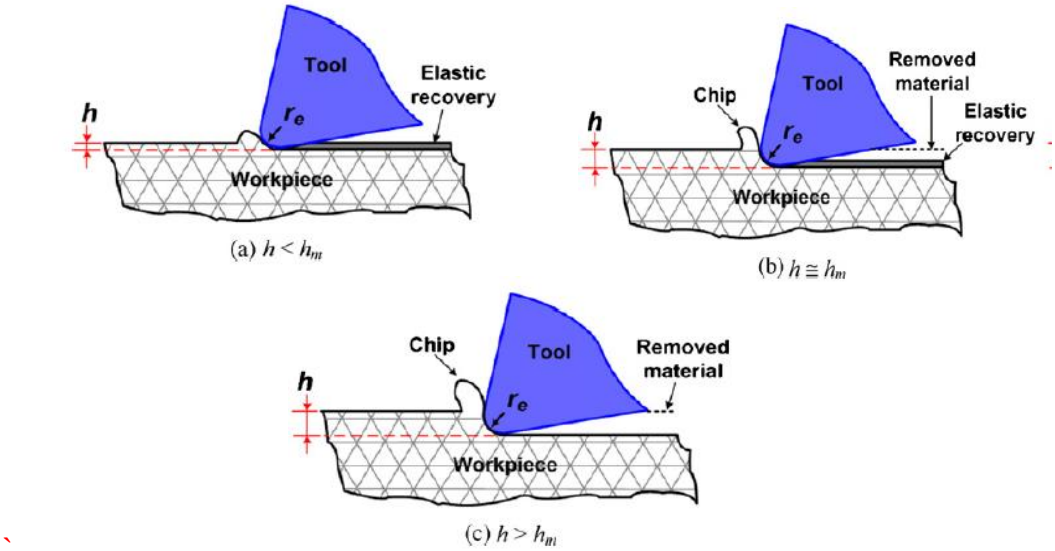

Figure 6: Chip formation in relation to the Minimum Chip Thickness threshold [16]

Several studies have worked towards establishing new models for micromilling in order to understand the mechanics of the process more accurately. Kim et al. [18] derived a theoretical orthogonal cutting model, taking into account the elastic recovery of the workpiece and the rounded cutting edge of the tool. Their orthogonal model is divided into 4 regions, as shown in Figure 7.

The first and the second region are two shear planes formed due to the round cutting edge. The third region is the friction region along the rake face of the tool and the fourth is the friction region along the clearance face of the tool and the newly formed surface of the workpiece. The incorporation of 4 zones gives a more realistic estimate for calculating cutting force and thrust forces. This "round edge model", as shown in Figure 7, explained experimental results for micromachining much better than the conventional merchant model.

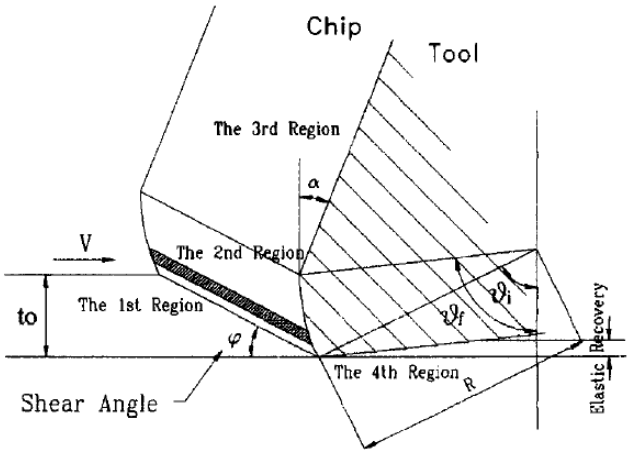

Figure 7: A round-edge orthogonal cutting model [18]

Kim et al. [10] created a theoretical model to account for the lack of formation of chips on each pass of a cutting tooth, especially at lower feedrates. They defined the ideal chip thickness as h_i and the actual chip thickness as h_a; the difference being the deflection of the tool when engaging the workpiece. What is found is that when the Uncut chip thickness is sufficiently high, shown as actual engagement h_a and feed per tooth h, in Figure 8 (a), each cutting pass produces a chip and the cutting is termed as a "steady cutting regime". Figure 8 (b) shows the condition where the feed per tooth h is much smaller, after the first cutting pass n=0, the cutting pass n=1 takes place in the non-cutting zone. This is the theoretical prediction based on the round-edged cutting model which show that the feedrate per tooth of the tool is significant in determining the chance of production of a chip. Similar studies have been done to derive and establish theories of micromachining and chip formation [11], [19]. It was found that as the tool wears out, the minimum feed per tooth required increases which should cause intermittent chip formation.

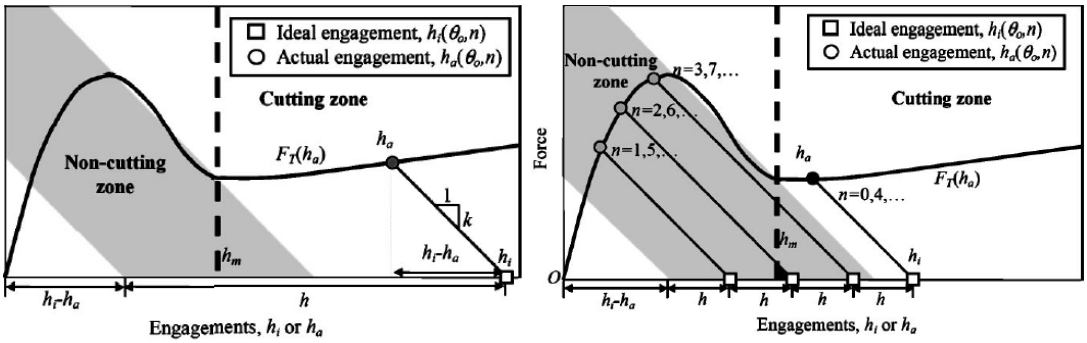

Figure 8: Comparison of impact of slow feedrate on cutting [10]

The value of Minimum Chip thickness is not a constant for all cases. The value of the MCT varies based on the cutting edge radius of the tool used and also on the type of workpiece material being machined. Kim et al. [10] experimentally found the MCT to be 22-25% of the cutting edge radius for a micro end mill of 600µm diameter and cutting edge radius of 3µm. In [20], Yuan et al. experimentally observed a similar result. It is concluded that the minimum chip thickness is approximately 25-30% of the cutting edge radius. The workpieces used in these studies were brass and aluminum, and brass is a candidate material for this research work. Therefore, the minimum chip thickness (t_c) is approximated to be 30% of the cutting edge radius (R_e) of the tool. This is shown mathematically in Eqn. (1).

$$t_c \approx 0.3 \times R_e \tag{1}$$

2.1.3 Machine Vision in Manufacturing

Computer vision or machine vision has become popular with many successful industrial applications. Its capabilities make it a powerful tool and hence can be used for multiple applications. Industries such as manufacturing, automotive, biomedical have successfully used machine vision for activities such as object recognition, defect recognition, welding, dispensing etc. [21]. Golnabi et al. [22] described the design process for industrial machine vision systems and their applications. Some key aspects to consider in the design of these systems are surrounding scene considerations, system

consideration, followed by development of image acquisition, image pre-processing and processing algorithm generation. They mention the possibility of using machine-vision system for offline inspection of cutting tools. Kurada et al [23] reviewed the application of machine vision for Tool Wear Modelling as an offline direct sensor. They reviewed various needs of the system such as type of lighting and digital image processing algorithms. The study focuses on inspection techniques for flank wear and crater wear of cutting tools based on surface texture information for determining tool condition. Their conclusion is that more research is needed for online application of machine-vision in industrial environments.

2.2 TOOL WEAR DEFINITIONS

It is necessary to clearly define tool wear of micro end mills in order to better understand the tool wear characteristics. Many changes can take place in a micro-endmill after machining begins, such as loss of material due to chipping, deposition of workpiece material (built up edge), fractures and crack formation and changes in tool dimensions [24]. Researchers have proposed many different definitions of tool wear based on these different types of changes in a tool.

Zhu et al. and Tansel et al. stated some broad definitions for tool wear in micromilling. Zhu et al. [25] defined wear as "the change of shape of the tool from its original shape during cutting", while Tansel et al. [26] have said that, "Any difference between a new and a used tool will be referred to as 'Wear'".

The different changes that occur in a tool lead to more specific tool wear definitions. Wear on the relief surface or clearance surface of the tool is called *flank wea*r. It causes formation of a '*wearland'*. Rubbing of this wearland on the freshly machined surface causes dimensional inaccuracy and poor surface finish. Flank wear is

common in all cutting processes and due to a significantly round cutting edge, the clearance surface tends to significantly rub on the machined surface. Figure 9 illustrates flank wear in various stages of a tool's life.

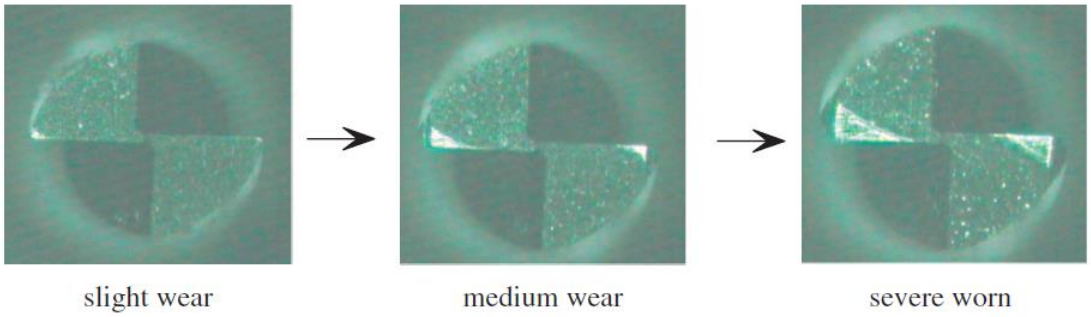

Figure 9: The progression of flank wear of the end mill [39]

Wear occurring on the rake face is generally in the form of chipping of the tool, and is termed as '*crater wear'*. It reduces the cutting lip angle, and weakens the cutting teeth. As micro end mills are extremely small and weaker than the macro tools, its life is adversely affected by crater wear. Due to the higher stresses and cutting forces in microscale machining, sudden and abrupt breakage of the tool is common. Tansel et al. [26] explored the reasons for breakage, and came to the conclusion that tool breakage mainly occurs due to chip clogging, which causes increase in cutting force requirement. Other reasons mentioned include fatigue breakage due to increase in the tool cutting edge radius which increases the cutting force, and deflections in the tool due to vibrations.

Another type of wear in micro end mills is the cutting edge wear or *'edge wear'*. This causes a change to the cutting-edge radius of the endmill. Micromilling cutting studies have focused on incorporating the round-edge model to understand the mechanics of cutting. This means cutting edge radius and edge wear are important

factors in governing the cutting forces and the thrust force acting on the tool. This in-turn governs the cutting parameters of the process.

A large edge radius increases the tool lip angle causing an effective negative rake angle and small clearance angle [16]. This suggests that an increase in the cutting edge radius results in increased flank wear. Therefore, the extent of flank wear is dependent on the cutting edge radius condition. Additionally, a change in the cutting edge substantially increases the forces due to increase in ploughing, friction and elastic recovery of the material. Wang et al. stated the reason for increase in this as the reduced ratio of the uncut chip thickness to the cutting edge radius [11]. This causes faster and less predictable tool breakage [26]. Cutting edge radius also has a direct effect on the chip formation process because of the minimum chip thickness effect.

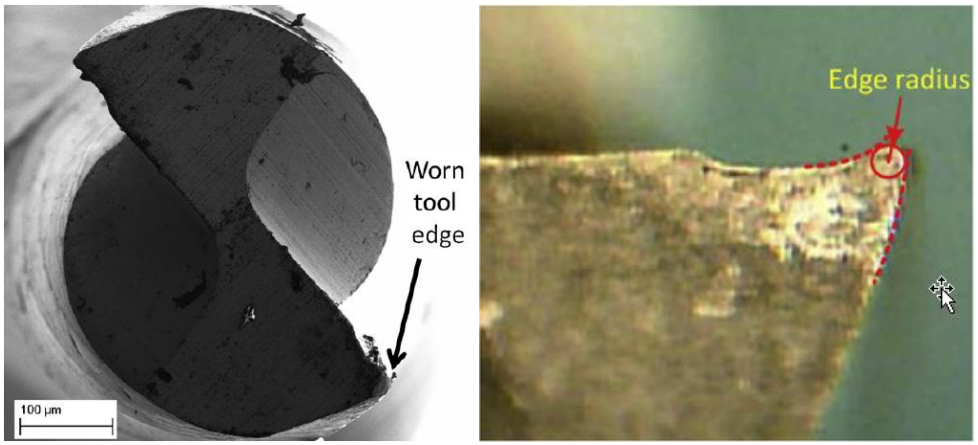

Figure 10: A worn cutting edge radius and the measurement method [13]

Unlike the macro tool, flank wear contributes very little to change in tool geometry in micro end mills [27]. Flank wear is measured in terms of the wear land area, and is used frequently in macroscale tool wear studies. However, in micromilling, measurement of the flank wear land is extremely difficult [28]. The cutting edge radius can be measured easily and more consistently. For these reasons, the cutting edge radius

wear is a more meaningful measure of tool wear for microscale tool wear studies. The experiments in this thesis will use this measure to classify tool condition.

2.3 TWM AND TCM SYSTEMS

Chapter 1 introduced TCM and TWM systems and their applications. These systems use various tool wear sensors. These sensors are required to be reliable, accurate and not interfere with the machining process. At the same time the data should provide strong correlation with the changing tool condition. There are two types of sensing methods, indirect and direct.

'Indirect' means that the parameter being measured can be correlated to tool wear, but does not reflect the ground truth of the tool or is not a parameter that can be measured on the tool. Cutting force measurements, acoustic emissions (AE), and vibration measurements are some examples of these measures. The downfall of this type of sensing is that indirect measures can sometimes be influenced by non-wear related phenomenon. Tool runout, spindle vibrations, and external conditions can adversely affect the AE sensing and cutting force sensing, which in-turn affects the effectiveness and capability of the TCM system.

A direct measure of tool wear is a tool wear signature which is directly related to the machining process. This measure is not affected by external conditions and hence can provide consistent information for a TWM system. Direct measures for TWM systems have been used at the macro-scale. The use of machine-vision based system to obtain images of the tool flank surface is shown in [23]. The use of proximity sensors, radioactive sensors is also documented. However, the viability of these methods at the micro-scale are yet to be explored.

2.3.1 TCM Systems

Some of the sensing equipment used by TCM systems are dynamometers for cutting force measurements, microphones for acoustic emission (AE) measurements and accelerometers for vibration sensing. Many algorithms have been used to gather the data from these sensors and generate a predictive capability for the TCM system via the process of machine learning. The limitations seen in current tool condition classification system is the lack of tool condition classification resolution. Resolution can be defined as the number of distinct tool conditions that can be accurately predicted allowing for multi-category classification. TCM systems rely on the predictive capability of the classifiers and algorithms to provide accurate results and have so far seen a maximum of three pre-defined states of tool: new tool (initial wear), used tool (wear progression) and worn (accelerated wear), being accurately predicted. The graph formed from this pre-defined criterion is referred by the researchers as Taylor's tool life curve.

2.3.1.1 Acoustic Emissions

Acoustic emissions are produced during cutting due to the plastic deformation of the shear plane, friction at the rake face and metal deformation at the flank face. Hence, changes in the AE signal can give an indirect indication of change in the condition of the tool. Jemielniak et al. [29], [30]. Observed that during cutting, AE signals are stronger in the beginning, weaker in the middle of the cut and often rise at the end. There are 'bursts' in the signal that occurred at the tooth passing frequency of the tool. AE signal amplitude is also found to increase dramatically as tool wear progresses [31]. When the data is transformed to the frequency domain from the time domain, the energy at certain frequencies is seen as peaks as shown in Figure 11. The

AE signals move to higher frequencies and lower energy levels with wear progression. AE signals also vary in amplitude with different feedrates [32].

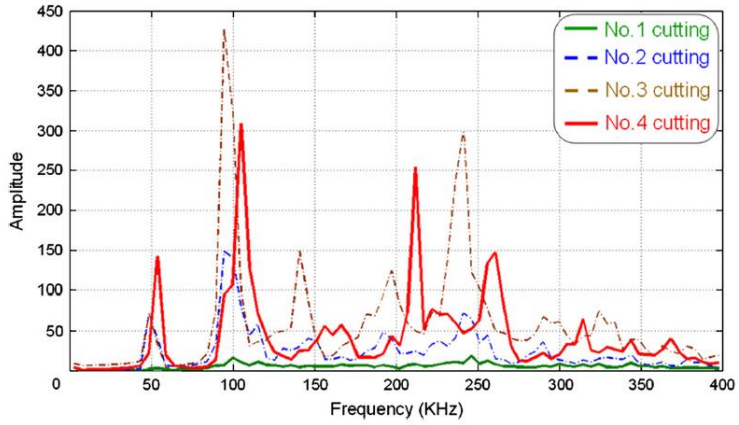

Figure 11: Frequency domain energy at different cutting passes [31]

Many other AE-based studies [28], [33]–[37] have shown similar trend of low to high shift of AErms values with a reduction midway through the cutting process was observed. Prakash et al. [34] attributed this trend to the small forces needed for chip formation while the tool is sharp. The reduction in the AE_{rms} values midway into the cut is attributed to the formation of build-up edge leading to inefficient machining. In the time domain, the AE_{rms} values increase with time. In the frequency domain, the energy levels at various frequencies is found to rise with each pass. The higher bandwidth of AE sensors allows measurement of signals correctly at high tooth pass frequency, which is ideal for the high spindle speeds in micromilling. These studies have reported a strong association between AE signals and tool wear progression.

2.3.1.2 Cutting forces

Cutting forces vary during the micromilling process and are an indicator of the tool condition. Cutting forces depend on factors such as tool cutting edge radius, tool geometry, shear angle, thrust force and tool helix start and stop angles [38]. The cutting forces are resolved into categories and attributed to the cutting or ploughing. The

ploughing and sliding force components are found to be higher when the uncut chip thickness is small. As this parameter is closely related to the cutting edge radius of the tool, cutting forces are an indirect indicator of the tool condition. Cutting forces have been found to increase in magnitude with increase in tool wear.

Zhu et al. [25] found that the cutting force signal magnitude is generally low and stationary with periodic impulses, as illustrated in Figure 12. Thus, effective signal processing and feature selection algorithms are required to eliminate noise. Figure 12 shows the relatively similar magnitudes of noise and the actual cutting force signal.

The next section explains some algorithms that use this data to predict the tool condition.

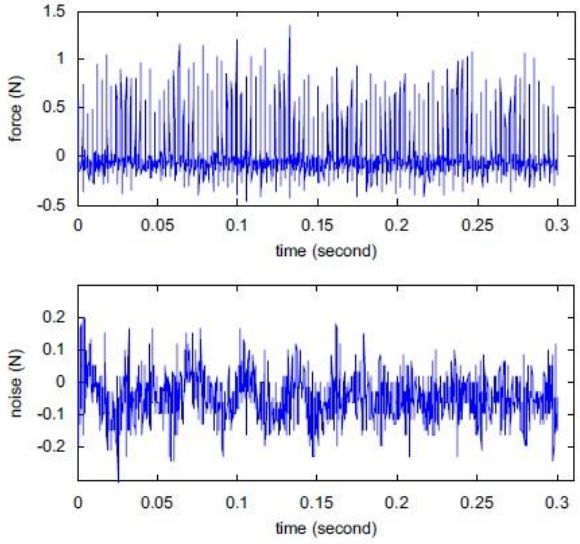

Figure 12: Force signal and noise component [25]

2.3.1.3 Algorithms

Among the two indirect tool wear signatures, AE signals have been found to be better than cutting force signals in several aspects: AE signals propagate at higher

frequencies than the characteristic frequencies attributed to machining. Hence, there is a much smaller noise component in the signal. AE sensors are also capable of capturing high-frequency vibrations due to availability of larger bandwidth in comparison to a Force sensor. Thus, a force sensor alone will not yield desired tool classification levels. Therefore, many studies have used a combination of the two sensors to collect more information. Many algorithms have been employed along with the use of single sensor or multi-sensor systems such as neural networks (NN) or hierarchical algorithms which have achieved varied levels of success in tool condition classification.

Kunpeng et al. [25] used wavelet analysis to obtain signal features for analysis from force signal data. A continuous Hidden Markov Model (HMM) was used to obtain a three-category tool condition classification by using flank wear as the defining criterion. They obtained an average classification success of 92.5% and 90.5% for machining of copper and steel respectively. In [39], Zhu et al. performed singularity analysis of the cutting force waveforms & the statistical analysis of the sudden shift in the mean value of the signal for their TCM. The assumption in this study is that the force waveforms generated are different for a sharp and a worn tool. They obtained 86-96% tool classification on a three-category scale defined using flank wear.

In [35], the same HMM algorithm was used by Lu and Wan, but data was obtained from an AE sensor instead. The resolution of classification was two level; sharp and worn. Signal features corresponding to the fifth tool pass were considered as worn tool, correlating to a flank wear of 38µm for a 700µm tool. They calculated a scatter index using a class-mean scatter criterion, which indicated the correlation of the signal features (SFs) to the tool condition. They obtained a 90-92% success in tool condition classification. Ren et al. [33] used Type-2 fuzzy logic to analyze AE signal

data. Different tool condition states were defined based on the AE_{rms} signal features, and selected signal features were integrated using a Type-2 TSK fuzzy approach to obtain a tool life estimate and the tool condition using a flank wear criterion. This approach enables them to estimate the tool life as well as the error of the estimation, as shown in Figure 13. The system predicted the tool state very well until 50% of tool life. However, the uncertainty in prediction increased in the latter stages of the tool life.

Yen et al. [31], [32] used AE sensors to obtain data during machining. They achieved accuracy of 100% for sharp tool classification and 80% to 95% for a worn tool classification. Jemielniak et al. [29] used AE sensor and Force dynamometers combined. The AE signals and force signals were compared to the physical condition of the tool at different time points of machining with the tool. In another study [30], they used data from AE sensors and Force dynamometers and used a hierarchical algorithm for their TCM system.

In the first stage of the algorithm, the tool wear is estimated separately for each signal feature and in the next stage, the results are integrated into the final tool condition evaluation. They concluded that signal features originating from different sources and more in number would eliminate the errors and give a better tool condition classification. Many more studies have been performed by Tansel, et al. [26],[37], [40]. In a subsequent research work [41], these researchers performed a similar study on non-metal workpieces.

The current TCM systems reviewed have seen good success in top level classification; a simple differentiation between a sharp and a worn tool. However, there is a significant dearth in the resolution of tool condition classification that can be obtained.

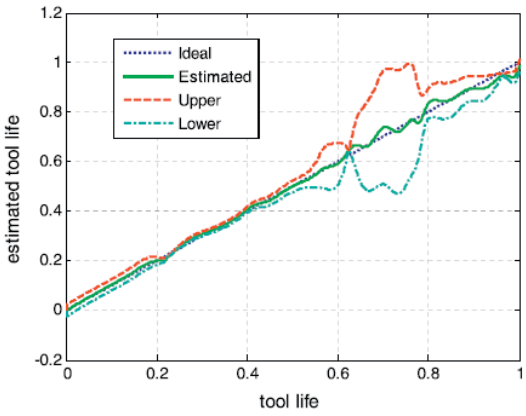

Figure 13: Tool life estimation [30]

2.3.2 TWM systems

All current TWM modelling efforts are performed offline by the use of Finite Element Analysis softwares for virtual modeling, and 'direct signature' sensing equipment such as scanning electron microscopes (SEMs) to observe and record the physical truth of the tool. Just like sensor fusion techniques in TCM systems, TWM system studies have sometimes performed both simulations and experiments to draw inferences on tool wear mechanics. The scope of these studies are generally narrowed down to some specific cases or applications and workpiece materials.

Some TWM studies have focused on analyzing the effects of different tool coatings and their effect on tool wear. In [42], Kumar et al. explored the performance of different tool coatings in laser-assisted micromilling of hard metals. They concluded that coated tools performed better and were capable of withstanding the elevated temperatures of the laser-assisted process. Li et al. [27] performed finite element modeling of a cutting tool by application of cutting forces, and compared the results to experimental modeling of the cutting process to optimize tool geometry and tool design of 2-flute square end mills for maximum tool performance. The parameters in question were tool helix angle and the cutting edge rake angle. Cutting tools with negative rake

angle and smaller helix angles performed better. Hamaguchi [43] performed studies on workpiece quality and tool wear of 2-flute ball end mills and the effect of tool tilting angle on tool wear. They used force signals to compare changes in cutting force to correlate the data with flank wear measurements made under an SEM microscope.

Most TWM studies involve performing experiments and the offline nature requires repeated measurements of the micro end mill under the microscope. The data is crucial to explore the process of micromilling under different conditions. This TWM system aims to establish a completely online method of this procedure by making an effort to establish the system and evaluate the hypothesis of the indirect signature that is proposed.

3 TOOL WEAR MODELING SYSTEM DESIGN

This Chapter describes the concept, development, and design of the Tool Wear Modeling (TWM) system which will be used to evaluate the hypothesis. Section 3.1 touches upon the development methodology and the high-level system and sub-system requirements and layout. Section 3.2 describes in detail the design and development activities of these sub-systems. This section both reports and expands upon work that was previously performed by a Capstone team of students at Arizona State University who implemented several of the required sub-systems as a senior design project. Section 3.3 discusses the system characteristics and the parameters that determine its operation. Section 3.4 describes the algorithms implemented for the working of the system.

3.1 DEVELOPMENT METHODOLOGY

In order to achieve the objectives and successfully evaluate the hypothesis, the system needs to collect the chips produced and return the chip count, or number of chips produced per unit time, in real-time. In order to accomplish this, the system needs a live chip extraction system. The variable of interest for the system is the chip count. In order to count the chips, a machine-vision system is implemented. However, in micromilling the expected number of chips produced per second is very large due to the requirement of high spindle speeds. Also, imaging systems require a steady field of view with consistent lighting conditions for imaging the chips. Hence, a motion and adhesion sub-system is needed to bridge the imaging and the extraction of chips.

If successful, the system will be able to extract chips in real-time and return a graph of the chip count vs time or chip count vs feedrate as needed. Figure 14 shows

the concept of the system, with labelling showing the different sub-systems. Our research group filed a design patent for this chip counting system [44].

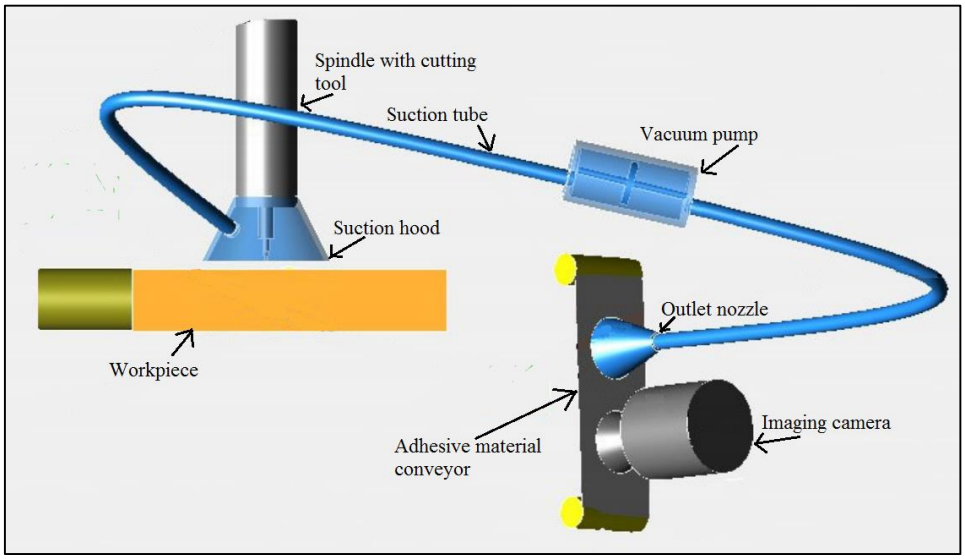

Figure 14: A concept overview of the chip collection and counting system [44]

3.1.1 Sub-system Requirements

As explained previously, the TWM system is classified into three functioning sub-systems. These sub-systems have the following requirements.

Pneumatic sub-system:

- Successfully extract all the chips being produced during the micromilling process
- Convey the chips to the motion and adhesion sub-system without any clogging and with minimal loss of chips

Motion and Adhesion sub-system:

- Successfully collect the chips conveyed from the chip conveying system with minimal loss
- Convey the chips to allow for quick image-processing and low system latency
- Generate a stable field of view for high-quality imaging

Image acquisition and processing sub-system:

- Capture a sharp and consistent image
- Pre-process and post-process the image to obtain an accurate chip count
- Provide the chip count in the form of a graph with respect to time

The proposed system can have some limitations. One problem is that it is difficult to effectively predict beforehand, any loss of chips from the system. It is also difficult to predict the flow of each individual chip in the system due to a large number of influencing factors.

3.2 SUB-SYSTEM DESIGN

3.2.1 Pneumatic sub-system

The pneumatic sub-system consists of five components: (1) a 'suction skirt' fitted around the micro-endmill, (2) a vacuum-based material conveying suction pump, (3) a suction tube connecting the skirt to the vacuum pump, and (4) a 'nozzle' which disperses the chips from the vacuum pump to the motion and adhesion sub-system. The system variables of this sub-system are: (1) Supply air pressure and the resulting flow, and (2) Length of suction tube.

Suction skirt:

The suction skirt creates a closed suction volume around the micro end mill. The skirt is fit to the bottom of a tool registration device and provides a physical containment for the chips produced. The skirt has a suction hole to which the suction tube connects. The size of the suction hole on the inlet skirt is large enough to allow for a high static vacuum and vacuum flow at the suction point. However, its size had to be limited to not damage the structural integrity of the suction skirt.

The suction skirt is positioned such that the skirt is approximately 0.5 to 1 mm above the tool tip. This provides a recess for atmospheric pressure air to flow into the area, which is necessary for suction of the chips. The suction skirt has the following dimensions:

Outer Diameter = 20 mm; Height = 6 mm; Vacuum Hole = 3.175 mm

Figure 15: (L to R): Front view and side view of the skirt and suction tube

Vacuum Pump:

Clogging and uneven dislodging of chips could cause erroneous results of chip count. Therefore, the vacuum pump is selected such that there is little possibility of clogging of chips. This vacuum pump operates on Venturi principle based suction generation, and has no internal moving parts. Pressurized air is input into an annular ring in the pump body. This air is ejected through nozzles on the internal side of the body which accelerates the air to supersonic velocity. This creates a vacuum resulting in suction on the inlet side. The input pressure helps regulate the transfer speed of solid material from inlet to outlet. The choice of such a pump is based on factors like required static vacuum pressure, velocity requirement and size of the material being transported. Based on this, the pump procured was the 'Vaccon DF 1-3' Venturi suction pump. A picture of this pump is shown in Figure 16.

The pump provides a maximum static vacuum of approximately 12" Hg (400 mbar) at 100 psi (7 bar) supply pressure. The air consumption is approximately 100 lpm (litres per minute), which is also the vacuum flow of the pump at that pressure. Compared to other variants, this pump provides the highest static vacuum and lowest vacuum flow at a given air supply pressure. This means it produces low velocities and large suction, which is desirable. More performance data pertaining to the pump is listed in Appendix A.

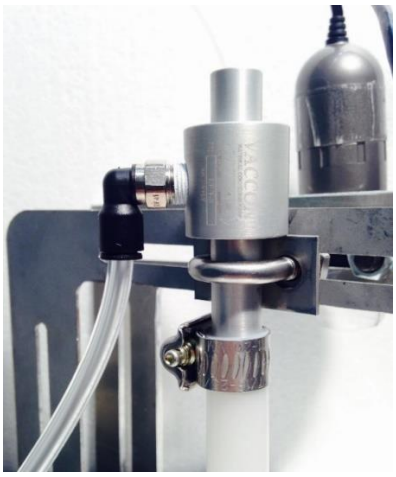

Figure 16: Vacuum Pump & outlet nozzle for chip suction

Inlet Tubing:

The suction tube connects the vacuum pump with the skirt. This tube provides a transportation path for the metal chips. The tube is required to not develop kinks or deformations as they can cause suction pressure drop. Wear and tear of the inside walls of the tube and a tendency to developing static electricity are undesirable. The tube material selected is polyethylene, which was selected by running trials with other candidate materials. The diameter of the inlet tubing is 3.175 mm or $1/8^{th}$ inch inner diameter. This was dictated by the inlet opening of the suction pump. It is much bigger than the expected size of metal chips. The vacuum flow available at the operating

pressure range of 40-100 psi ensures a very high air transport velocity into the pump, which reduces system latency.

Outlet nozzle:

The nozzle disperses chips from the pump onto an adhesive surface, which is a part of the motion and adhesion sub-system. The function of the nozzle is to prevent chips from being lost and to evenly disperse chips across the width and within the confines of the adhesive material. The outlet nozzle diameter was dictated by the outer diameter of the pump outlet, and the width of adhesive tape available in the market. The inner diameter is 12.7 mm (1/2”). This relationship in tubing diameters is important in order to increase the air velocity where the chips are being pulled into the air stream, which will help prevent loss of chips due to spindle scatter and not cause the chips to stagnate or clog. Decreasing the air velocity where the chips are being pushed out of the air stream onto the adhesive material will prevent loss of chips due to dispersion. A four-fold increase in the tubing diameter ensures a sixteen-fold decrease in velocity at the outlet. A hood/ cover is attached at the bottom end of this exit nozzle. The function of this is to avoid any effects from external air circulation.

Air flow and pressure:

The pneumatic system is driven by a single pressured line that provides pressurized air for the vacuum pump and air bearings of the spindle. The static vacuum generated by the pump increases almost linearly in relation to the pressure of supply air. The vacuum flow varies in an inverse exponential manner with increasing supply pressure, and remains constant at a maximum of approximately 100 lpm after 30 psi of supply pressure. For initial experiments, the pressure is set to be the maximum rated

pressure, 100 psi. In the latter experiments, air flow at different pressures was tested to determine the optimum pressure.

3.2.2 Motion and Adhesion sub-system

The motion and adhesion sub-system consists of a conveyor belt that is used as the base to move a strip of adhesive material under the nozzle and past the imaging system. Other components are an adhesive tape roll, a roller wheel to source the adhesive material from, and another roller wheel to collect the adhesive tape and remove it from the belt. Important design considerations for this sub-system include: control of belt speed, choice of adhesive material, positions of the rollers for the tape, belt color and reflectivity, and torque of the motor providing tension in the tape at the collection roller.

A conveyor belt for this purpose was donated by Misumi, Inc. The conveyor belt is a variable-speed belt with a range of 1.3 to 34.5 m/min. The belt is of white matte (non-glossy) color which would prevent direct reflections off of the belt, as well as provide contrast to the darker-colored metal chips. The speed of the belt is controlled by an analog voltage input, varied using a microcontroller. The belt motor is equipped with an encoder to read out the belt speed. It is crucial to know and set a desired belt speed in order to predict the number of chips expected per picture captured by the imaging sub-system. The output of the encoder and the input to the speed control are both wired to a PSoC microcontroller. The PSoC is connected and operated by the same computer that also operates the imaging sub-system.

There were two candidate adhesive materials. One was a transparent double-sided tape obtained from ‘McMaster-Carr’, and the other was a 3M heavy-duty wall mounting tape; both the tapes being 1 inch in width. After initial experimentation, the

opaque white tape is chosen for the system, as it has a much smoother surface which provides better image quality. It is also less prone to wrinkles and folds as it is much thicker than the transparent tape.

The tape is positioned on the roller in a manner to allow the weaker adhesive side to roll on the surface of the belt, which allows easy removal from the belt after imaging is performed. The stronger adhesive side faces the nozzle to capture chips being released. Also, the tape roll is positioned such that it is rolled off parallel to the belt surface in order to avoid creases on the tape.

The tape is peeled off the belt on the other end by a 12V DC motor driven roller wheel. The motor torque estimation was performed experimentally by using a spring with a known spring constant, wherein one end of the spring was attached to the tape on the belt and the other held stationary. The deflection of the spring before the tape started to peel off provided an estimate of the adhesion force. This motor is also controlled using the same PSoC in order for the belt and roller to operate at the same linear speed.

This selection of the components in the motion and adhesion sub-system was influenced by the pneumatic sub-system, which is downstream. The belt color and the color of the opaque tape are white as the workpiece material chosen for the experiments is brass, which stands out more visually against a white background than against a black background. Commercially and economically available adhesive tapes have a width of 1 inch, which is larger than the outlet diameter of the nozzle (0.5 inches). The belt speed is determined based on the chip production rate of micromilling. The choice of this parameter however, also depends on the capability and/or limitation of the camera in

terms of its framerate and resolution, which are constrained by cost. The details of selection of the optimum belt speed is given in Chapter 4.

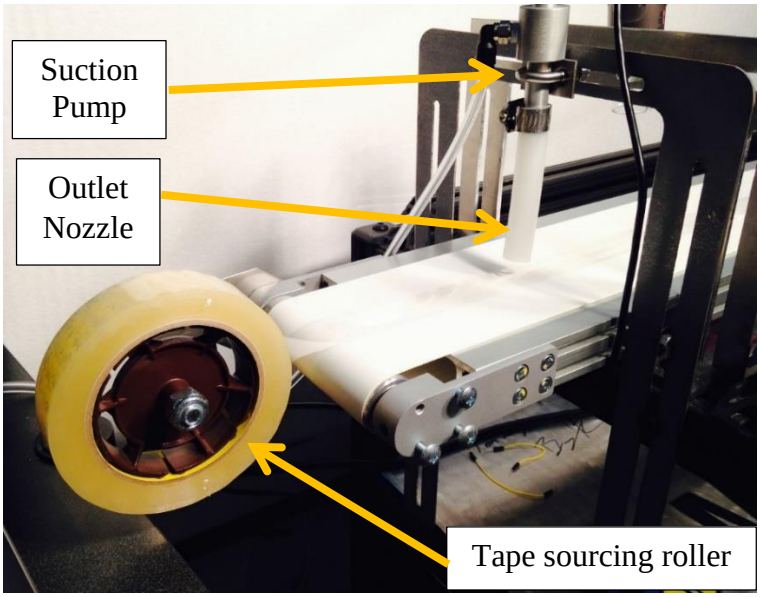

Figure 17: Picture showing the motion and adhesion sub-system

3.2.3 Image acquisition and processing sub-system

The image acquisition and processing sub-system consists of two components: (1) an image acquisition device (USB microscope) and (2) image processing algorithm running on MATLAB®. The camera is mounted on an adjustable mounting bracket to allow for greater functionality of the camera in terms of setting the correct working distance (WD) and field of view (FOV). The image acquisition device selected is a USB microscope. A regular digital camera lacks sufficient magnification to observe the chips, making the USB microscope more desirable for this purpose. The selection of the USB microscope is influenced by three main factors: the chip size, number of chips expected per frame and size of adhesive tape. These parameters affect the resolution, magnification, framerate and lighting requirements of the microscope. The camera

requires enough resolution to identify each chip uniquely. The resolution also cannot be very large as it would make the system computationally slow.

The chip production rate, or number of chips produced depends on the cutting tool spindle speed, N. The camera should be able to image the maximum number of chips produced, i.e. when the MCT threshold is not violated. Another requirement is the FOV setting of the camera. The size of the adhesive tape dictates this setting. The camera must be able to image all the chips across the full dimensions of the adhesive tape. Therefore, to calculate the minimum resolution requirement of the camera, the maximum chip size is calculated and a square box of the largest dimension of the chip is considered as the area of an image a chip will occupy.

The system is designed such that one chip must occupy an 8-neighbourhood of pixels (3 pixels in each direction). Another condition that is taken into account is to preferably have these chips, a minimum of an 8-neighbourhood of pixels away from each other in order to reduce the likelihood of chip overlap. This means that a single chip must occupy 81 square pixels to assure identification of each chip separately. This is shown in Figure 18, where the yellow chip will occupy the full yellow grid, and the red area is the area that it should preferably occupy.

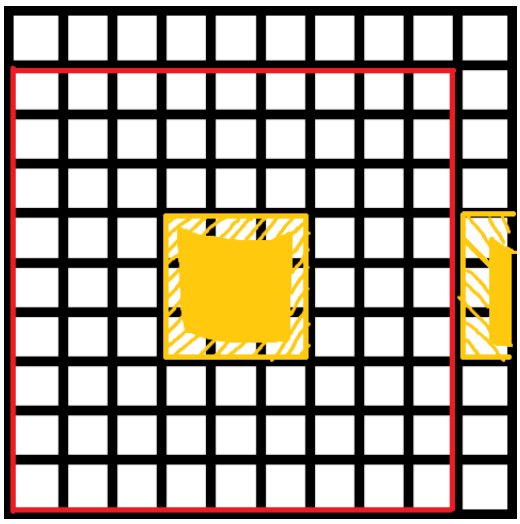

Figure 18: A pixel grid showing the metal chip and the 81-pixel neighborhood

However, it would be incorrect to assume that the density and orientation of the chips on the conveyor belt will be even on the entire frame. It is possible that chips will be laid over one another. Hence, a much larger pixel-area requirement per chip is needed to be able to identify each individual chip successfully. These parameters then dictate the minimum required framerate capability of the camera. The framerate has to be large if the number of chips imaged per frame is small. This factor is found to dictate the operating speed of the conveyor belt while running the TWM setup. These equations and relations are derived in Section 3.3.

The choice of lighting for the experiment is crucial and it influences the subsequent step of image processing. The initial concept for image acquisition used a strobe light to provide repeated bursts of light at a set frequency. The idea was to be able to run the belt at a set constant speed and based on the requirement of frames per second, the strobe light would flash at a set frequency. This would eliminate the problem of image blurring due to a moving belt. However, a digital video device refreshes the image row by row rather than frame by frame. Thus, images taken under the strobe light sometimes end up being part-lit and part-dark as shown in Figure 19. Countering this would increase the framerate requirement of the microscope, making it too expensive.

Therefore, the light chosen is a 1000W flood light. This bright and powerful light provides consistent high contrast images. However, for the system to work properly, the belt is stopped at specific instances to grab a still frame and avoid image blurring. The light is also placed such that it is looking almost vertically down on the

belt to avoid shadows of the chips degrading the image. The rest of the room is kept dark to not interfere and have better control over the lighting conditions in the room.

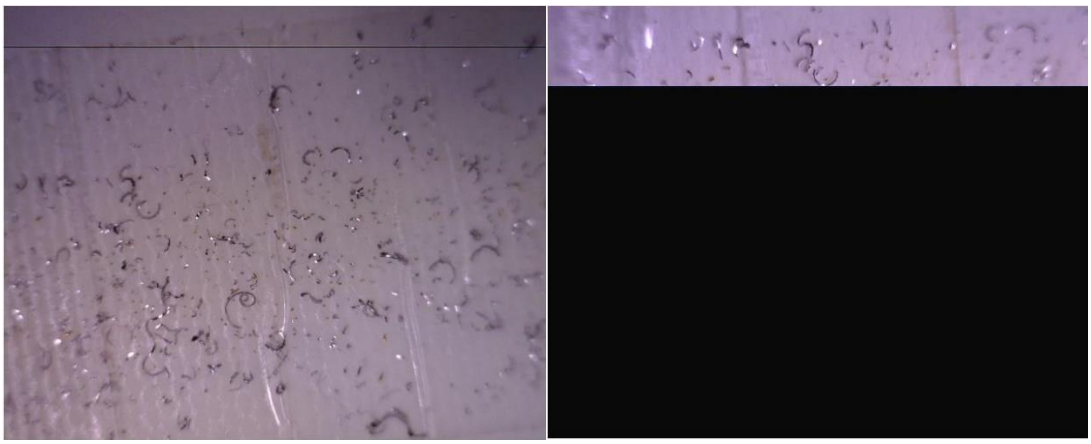

Figure 19:Images taken using a strobe light; highlighting both possibilities

3.3 SYSTEM OPERATING PARAMETER SELECTION

Figure 19 shows the working of the TCM system in a system breakout. The system is characterized by deriving governing equations for the operating variables such as belt speed, air supply pressure and so on. These equations are used to control the variables in order to obtain desired and predictable performance from the system. The functioning of the system is then decided as an optimization problem of the variables to obtain the desired operating point.

Due to the small size of cutting tools, the spindle speed (N) for micromilling is generally kept high to meet the cutting speed requirements and develop the necessary cutting forces. The cutting speed can be as high as 80,000 rpm in the spindle available. The cutting tools used are two-flute micro end mills, which have 2 cutting teeth (n).

The maximum chip production rate (C_r) in the process is determined by Eqn. (2). At the spindle speed of 80,000 rpm, 2,666 chips are produced per second.

$$C_r = \frac{nN}{60} \tag{2}$$

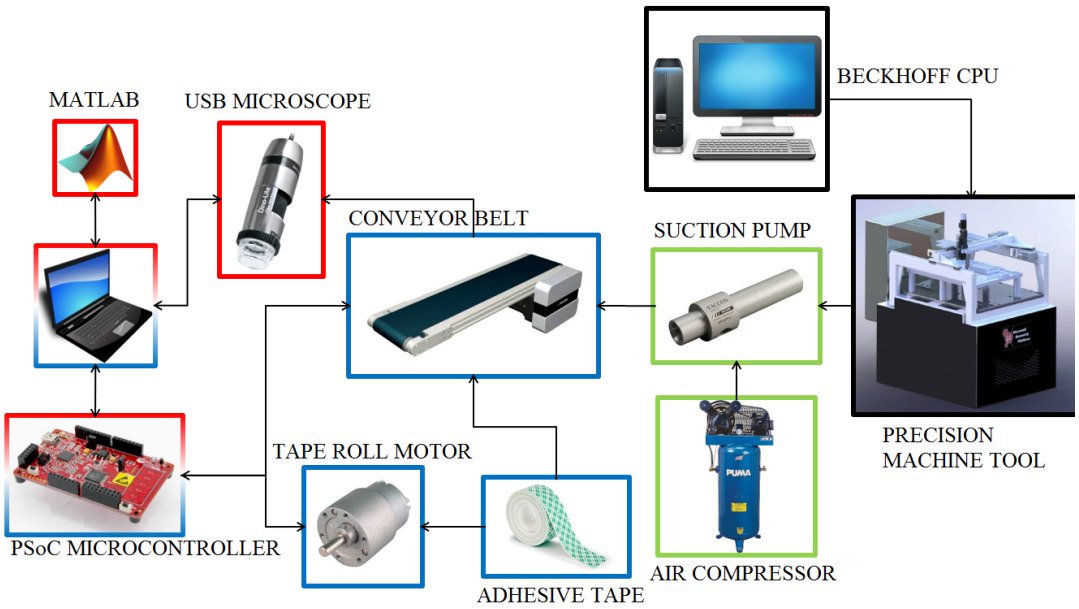

Figure 20: Sub-system work-flow of the system: Green (Pneumatic), Red (Imaging), Blue (Motion)

The size of chips formed in the cutting process depends on axial depth of cut (d), feedrate (f), and the diameter of the cutting tool (D). A chip can have a maximum length (L) equal to an entire single pass of a cutting tooth. This is reflected in Eqn. (3).

$$L = \frac{\pi D}{2} \tag{3}$$

The relationship in Eqn. (3) is prone to vary based on the physical properties of the workpiece such as hardness, ductility etc. A study on chip morphology found that the average chip formed when cutting with a 150 µm tool was found have 11 ‘segments’ of 5µm and hence the chip size was 55 µm [11]. The chips produced are picked up by the pneumatic conveying sub-system and are dispersed on the adhesive tape. Combining the belt speed, chip dispersion area, and chip production rate gives an “expected” number of chips per image which can be compared with the actual count obtained.

For the imaging sub-system, the USB microscope has a resolution of 1.3 MP (1280 x 1024) and a frame rate of 15 frames per second. However, the bottleneck of the imaging sub-system is the time it takes for the computer to process the image. This sub-system depends on some other variables that determine its operating point viz. size of the chips and chip production rate. The chip production rate can be a deciding factor in determining the minimum framerate. However, since it is not required to capture every frame, this is not a constraint. The field of view (FOV) is dictated by the width of the adhesive tape. It is possible to adjust the working distance (WD) and the magnification of the microscope to comply with this constraint. However, the relatively low resolution of the microscope puts a limit on how big the working distance can be. Hence these operating variables are interdependent, as shown in Figure 21

The Field of view available in the X and Y directions can be taken as FOV_x and FOV_y. The adhesive tape is 1 inch or 25.4 mm in width. Thus, FOV_y = 25.4 mm and FOV_x = 25.4 x (1280/1024) = 31.75 mm

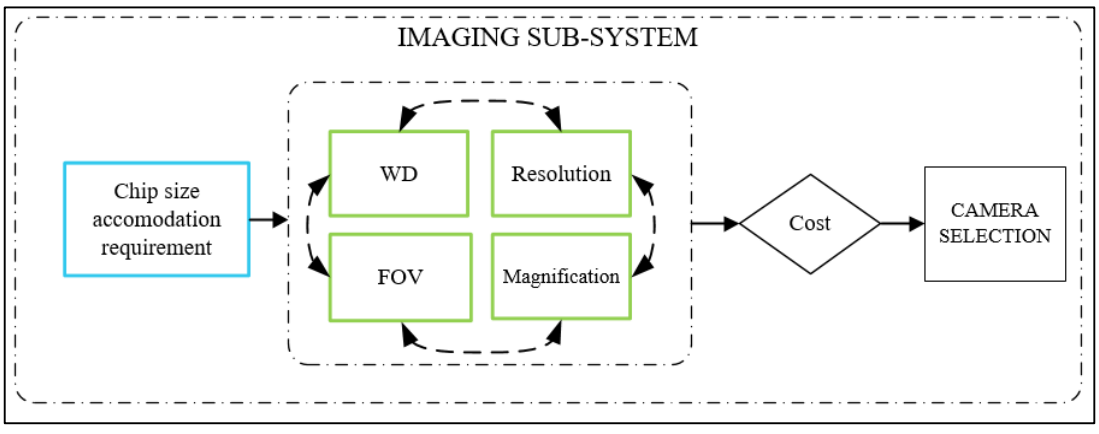

Figure 21: The variables of the Imaging sub-system

By using the FOV and resolution information, the dimension for each pixel is calculated to be 24.8 x 24.8 μm. It was pre-determined to perform experiments with micro end mills of 200 μm. Wang et al. [11] found the average length of chip (L) produced by a 150 μm tool is 55 μm. Therefore, we assume an average chip size larger than that. Thus, the theoretical maximum number of chips that can be fit per frame (N_f) is given in Eqn. (4), which in this case comes to approximately 200,000.

$$N_f = \frac{\left(FOV_x \times FOV_y\right)}{L^2} \tag{4}$$

However, as discussed before, it is a minimum requirement for a chip to occupy 81 pixels (9 pixels in each direction) to identify each chip separately. This is defined as the chip area. Hence, the maximum number of chips per frame comes to approximately 16,000 which is calculated using Eqn. (5)

$$N_f = \frac{(FOV_x \times FOV_y)}{Chip\ Area} \tag{5}$$

The theoretical value of 16,000 chips per frame may not be possible in practice, due to the stochastic nature of chip dispersion. Also, it takes a minimum of 5 seconds to generate approximately 16,000 chips. The sampling rate of the TWM system needs to be much higher than that. Thus, the actual number of chips that can be successfully imaged will be determined experimentally by keeping image quality and sampling rate requirements in mind. This however means that the USB microscope is capable of the task and will not be a bottleneck on the system.

The motion and adhesion sub-system has a conveyor belt with a speed (V) range of 21.6 mm/s to 576 mm/s. Since the outlet nozzle diameter is 12.7 mm, it can take a maximum of 0.58 seconds to pass over the nozzle. The size of the image in this direction

is *FOVx*, which is 31.75 mm. Hence at the slowest speed, the number of chips per image (N_f) is equal to 4,000 chips per image. This is calculated using Eqn. (6).

$$N_f = \frac{(FOV_x \times C_r)}{V} \tag{6}$$

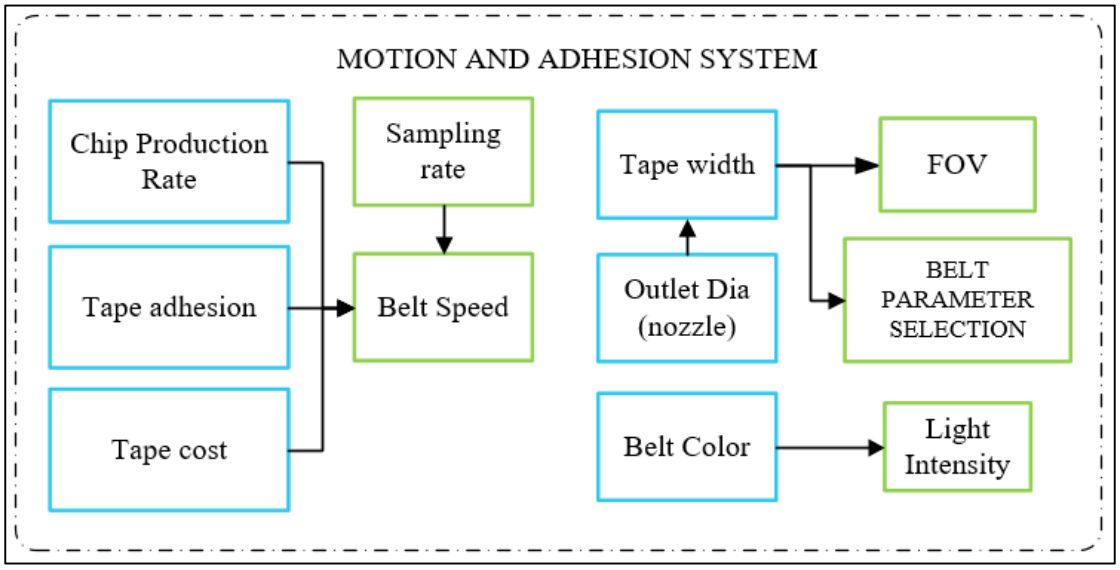

Figure 22: The variables of the motion and adhesion sub-system

However, the belt speed selection is influenced by other requirements such as tape adhesion and the cost of the tape, as shown in Figure 22. The belt speed has to be large enough in order to generate the required force to overcome the adhesion of the tape and roll it on smoothly. The sampling rate of the system depends on the belt speed setting. A faster belt implies a higher sampling rate. However, a belt speed too fast will consume adhesive tape much faster which proves costly. The belt speed is chosen in order to account for these considerations, as it is a crucial variable that determines the performance of the system in terms of the sampling rate, chips per frame and the cost of experimentation. The selection calculation is shown in Chapter 4.

3.4 ALGORITHMS

The sub-systems are required to capture a frame when the belt stops, and process that image. Hence algorithms are designed to provide communication between the motion and adhesion and image acquisition and processing sub-systems. The algorithm and the logic diagrams are given in the following sub-sections. The actual code and scripts are given in Appendix B and C.

3.4.1 Motion sub-system controller algorithm

The motion and adhesion sub-system is required to run at a set speed and have a stop-start running cycle. The imaging sub-system takes a picture while the belt is in a stop condition. The belt speed setting is limited by the requirement of a sufficiently high sampling rate, but also by the cost of adhesive tape. The belt also has to traverse a minimum length between stops; the length being equal to the distance between the nozzle opening and the camera's frame.

The PSoC provides the capability for PWM –based control of the two motors: the conveyor belt motor and the adhesive tape roll motor. This is programmed in the PSoC creator environment. PWM blocks for the two motors are created to define the variables. The pin connections define the I/Os of the system. The logic of the code development is shown in the flowchart in Figure 23.

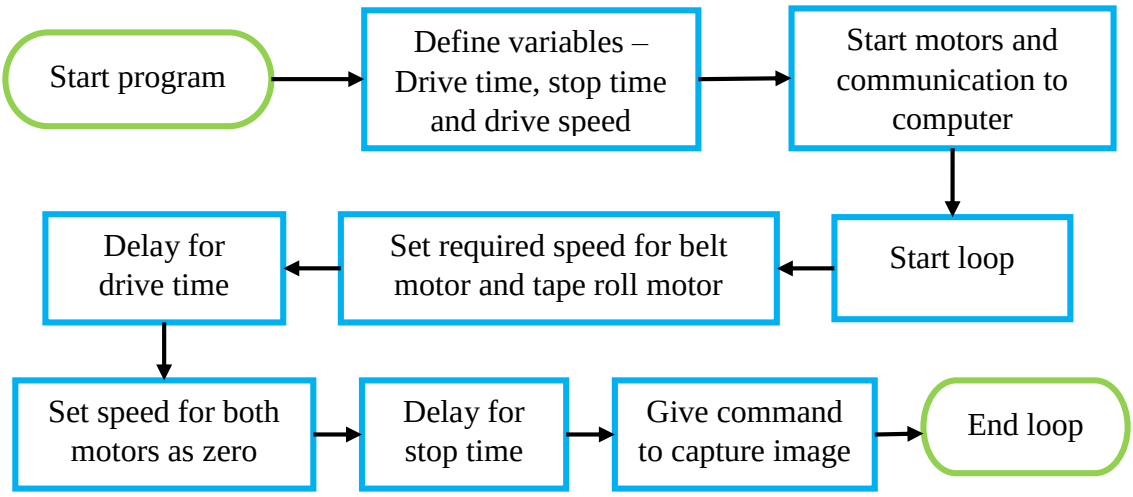

Figure 23: Flowchart of the logic diagram for the PSoC controller

3.4.2 Image processing algorithm

The imaging sub-system algorithm is developed using the Matlab image acquisition toolbox and the image processing toolbox. Initial testing for the algorithm was done using different sized chips such as those produced from a 1mm facing tool and also from the tool of choice, a 200µm tool as shown in Figure 19 in section 3.2. After choosing the preferred lighting and adhesive tape and using only the chips produced by the 200µm tool, the image processing algorithm was modified.

The first step of the image processing algorithm is to convert the captured color image to grayscale. A color image consists of much more data, with three 8-bit values per pixel, representing the R, G and B components in a 3-D matrix. It is not possible to convert this 3-D matrix directly into a 2-D binary scale matrix. Matlab provides maximum image processing capabilities in the binary format. The image is therefore converted to an 8-bit grayscale image with a minimum intensity of 0 representing the color black and maximum of 255 representing white. After conversion, the image shows that while the background is lighter and the chips are darker in comparison, there are some chips that are very bright as they are reflecting light directly at the camera due

to their lustrous nature. Therefore, the next step is the global thresholding of the image histogram. Thresholding leads to definition of a maximum or minimum intensity limit of all pixels in the image. The belt is found to have an intensity varying from 120 to 150 on the 0-255 scale, while the lustrous chips have an intensity of at least 180 or more. Thresholding operation blackens the lustrous chips by setting all values above 180 equal to 0.

After thresholding, the image is cropped. This is done in order to eliminate the outside borders of the image. The microscope when operated at the required WD and magnification leads to uneven focusing of the image. The center of the image remains sharply in focus whereas the edges of the image appear blurred. The contrast between a chip and the belt color in this blurred region is extremely low, meaning some parts of the tape and some chips are undistinguishable. This leads to a lot of image noise upon application of image segmentation operations. Image re-sharpening algorithms in Matlab are also not suitable for this application as they work by changing the contrast of the image to make the low values lower and the high values higher. With insufficient contrast, this leads to wrong results. To evaluate the image, we can find the total number of chips in that given area which will indicate the total number of chips in the entire image, assuming an even spread of chips across the field of view.

The image's grayscale threshold is calculated next in order to obtain a black and white image. The black and white image is a binary image, meaning the 0-255 values get converted into either 0 or 1 based on whether they are below or above the threshold, 0 for black and 1 for white. A negative of this image is then obtained.

The black and white images are found to have some pixelated errors or noise, especially in the image corners. These are generally single pixels, much smaller than the chips. Hence a morphological ‘cleaning’ operation is performed which removes these single pixels. The noise or errors which are bigger than a single pixel are tougher to deal with. However, this noise is found to generally be much more condensed in terms of its spread on the frame in comparison to the chips. Also, sometimes the metal chips have uneven lighting on their surface. A part of the chip might be better lit than the rest. Therefore, the metal chip pixels are sometimes converted into black or white, which reduces the number of pixels representing one chip. For these reasons, an image dilation operation is performed.

A dilation operation uses a structuring element of pre-defined shape and places this element on the picture, pixel-by-pixel. Any object smaller than the size of the structural element get enlarged to fit the size of the element. A square of 2 pixels by 2 pixels was chosen. Hence any chips that are smaller than 4 pixels are enlarged, and the cluster of noise gets aggregated into bigger chunks.

At this point, the image is of sufficient quality to perform the final step, which is a connected component command used to calculate the number of chips seen in the image. This command simply counts the number of connected components (represented by chips) in the frame. This returns the number of chips which is then plotted. As these images are taken in and processed chronologically, we can obtain a graph of chips vs time. A flowchart representing the logic of the image acquisition and processing algorithm is shown in Figure 24. Following this, a set of images are given that illustrate the step by step transformations performed on the actual images. This process takes place for every image that is captured.

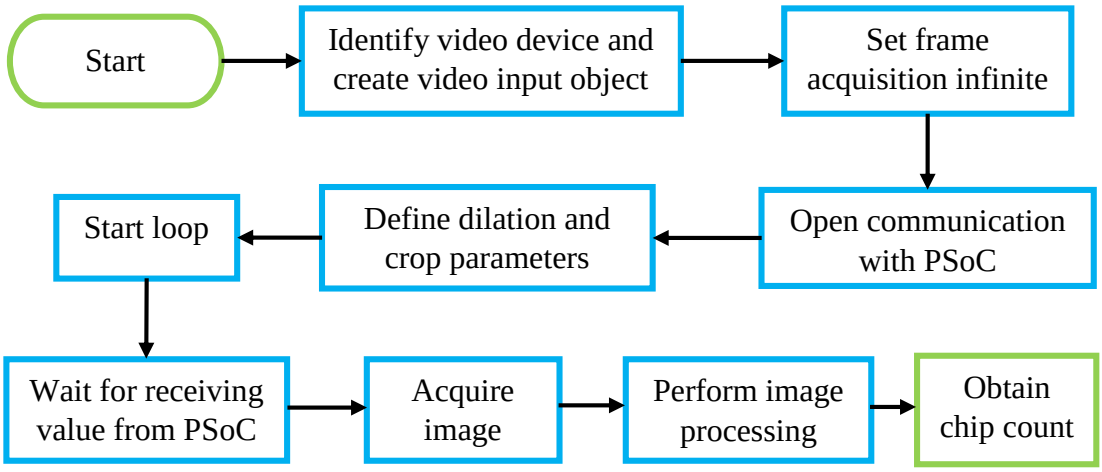

Figure 24: A logic flowchart of the image processing algorithm

Image 24 (a) is a typical picture that is captured by the microscope from the adhesive tape. The metal chips are a slightly darker golden color than the lighter belt, or are shining due to luster. Image 24 (b) is a grayscale conversion of the image. Image 24 (c) represents the crop and threshold transformation applied on the image. The metal chips are now seen as black specks on a light gray background. Image 24 (d) shows the black and white version of the image, which is converted to its negative in image 24 (e) for better viewing. After applying the morphological operations such as cleaning, and image dilation, we obtain image 24 (f). It is seen that the metal chips are visibly clearer, and the noise seen in the top left corner is slightly aggregated. A simple counting operation returns the chip count which for this case, is 440.

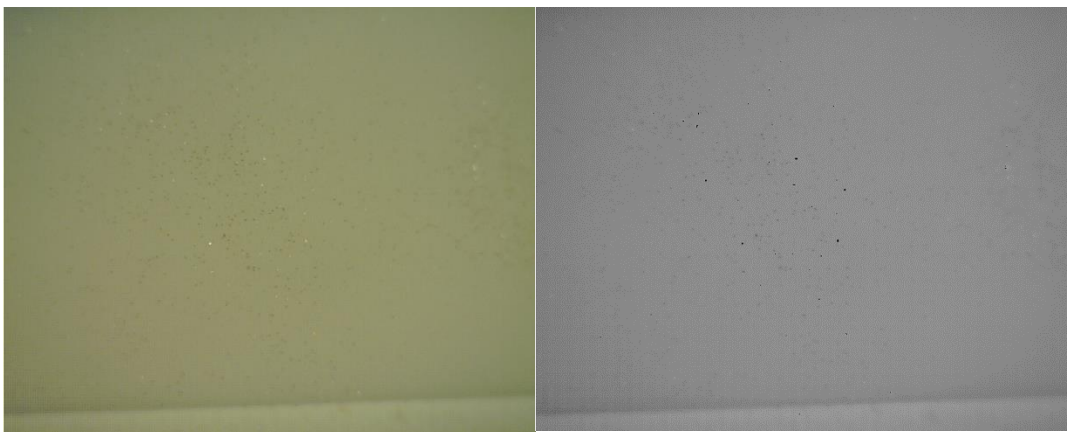

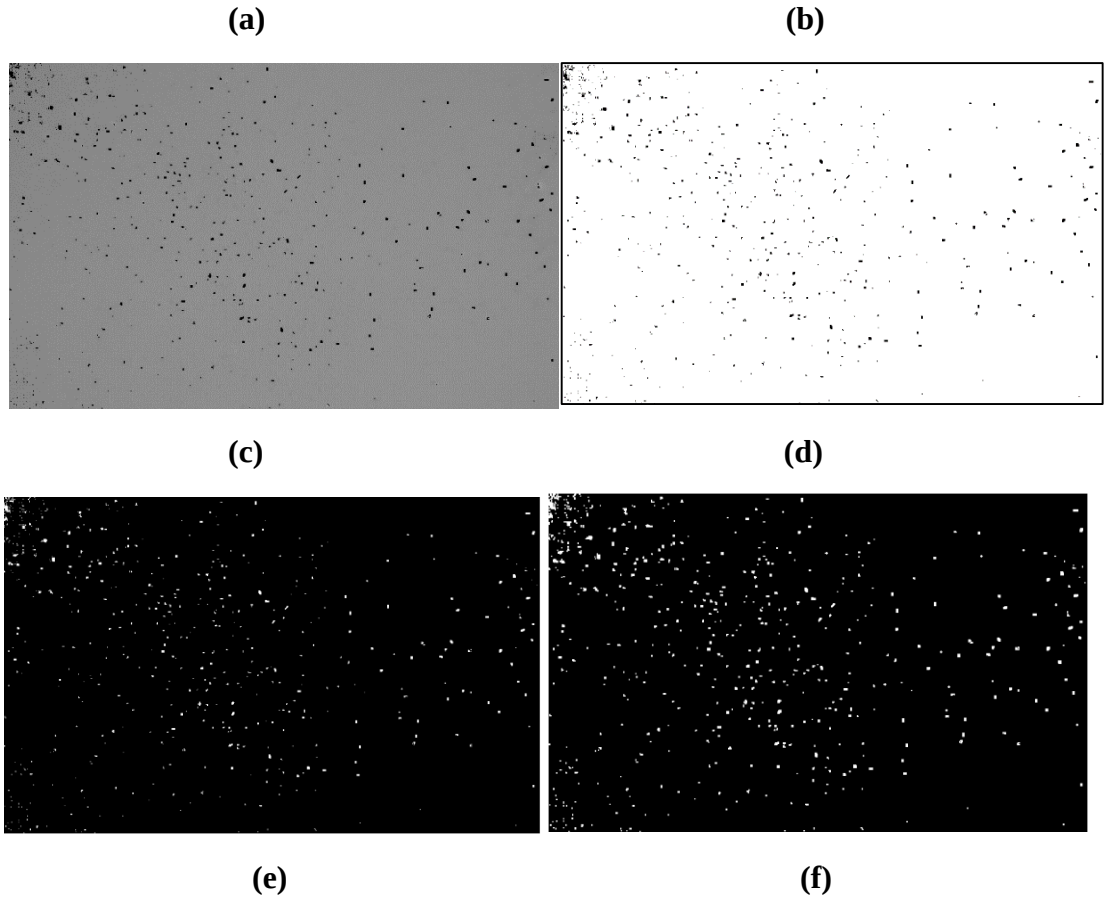

Figure 25: Series of images showing the various image processing steps (L to R), (T to B)

4 EXPERIMENT DESIGN AND PLAN

This Chapter describes the experimental plan and design to evaluate the hypothesis. Section 4.1 outlines the experiment variables. Section 4.2 describes the design of two experiments that are performed and the expected result from the experiments. Section 4.3 lists the various equipment used in the experiment.

4.1 EXPERIMENT VARIABLES

Independent variables:

These are the variables that will be varied during the experiments.

1. Feedrate (F):

The feedrate of a cutting tool is the velocity with which it is advanced against the workpiece. In micromilling, this variable is crucial for determining the possibility of producing a cut, and hence will be varied to test the hypothesis. This variable is calculated in terms of linear distance per time, based on the minimum feed value using Eqn. (7), and fed to the machine tool in millimeters per second.

$$F \geq 0.3 \times r_e * n * N \tag{7}$$

2. Cutting time (t):

The cutting time is the amount of time that a tool has been in contact with the workpiece while actively cutting. As the cutting time increases, the amount of tool wear will increase as well. The value of cutting time will increase therefore increase continuously as cutting progresses in all experiments. By varying the cutting time of a single tool, the amount of tool wear is indirectly varied.

Control Variables:

These are variables that are chosen before the experiments and kept constant.

1. Tool Diameter: (D)

The tool diameter choices have varied in previously-published micromilling research. The minimum tool size available commercially is 25 μm in diameter. The maximum tool diameter is undefined due to the ambiguity and lack of a clear definition of what can be regarded as *micro-scale* milling, although the maximum is generally taken to be around 1mm. Tools of 2 mm diameter are often used for facing operations on the workpiece. For the experiments, we have chosen to use a 200 μm tool. The tool is large enough to resist random tool breakages, and small enough to truly test the micro-scale effects.

2. Number of cutting teeth: (*n*)

A variety of end mills such as D-type, Δ-type and 4-flute tools have been used in some research works [45]. The most common, however, are 2-flute end mills. They are also of two types, ball end and square end mills. They are categorized by flute-length as stub-length and standard-length tools. A 2-flute stub length endmill is suitable for the purpose of these experiments as ball end mills are suited for machining in full 3-dimensions, while we will be cutting in only 2.5-dimensions, and standard length tools are useful for deeper cuts.

3. Spindle Speed: (*N*)

Unlike the macro-scale, the spindle speed cannot be estimated using The Machinery's Handbook [9]. The calculations based on the handbook would suggest extremely large speeds. In current systems, the speed is dictated by the spindle capabilities rather than the calculated values. The top speed of the spindle is 80,000 rpm, which will be set constant during experiments.

4. Belt speed (*V*):

The belt speed depends on the chip production rate of the process and the number of data samples desired. This variable will be kept constant for all the experiments. The cutting time per pass for all the experiments is expected to be a minimum of 8 seconds as the workpiece is 25.4 mm long and the maximum feedrate we will use is 3.2 mm/s. A faster belt will allow a higher sampling rate, but it will consume adhesive tape much faster as well. Figure 22 of section 3.3, shows that the four factors that will affect belt speed selection are chip production rate, tape cost, tape adhesion and required sampling per cutting pass. The sampling rate is the critical requirement.

Experience using the imaging system suggested that a time of 1.2 seconds is needed to have the belt come to a halt, and for the computer to capture the image and process it. Therefore, the belt travel time for the distance from the nozzle outlet to the center of the camera is minimized to 0.8 seconds, by setting the belt speed as 139 mm/s. This yields a minimum of 4 pictures per cutting tool pass at a high feedrate and also consumes the tape economically. The sampling time will be 2 seconds.

5. Depth of cut (z):

The cutting tool in use is a stub length cutting tool, which has a shorter flute length. A shorter flute length reduces tool deflection and increases tool strength. They are therefore suitable for operation involving small depths of cut. However, the depth of cut is kept large enough to negate the effects from any irregularities in the workpiece surface.

6. Workpiece material:

The choice of workpiece material affects the progression of wear of a cutting tool. Materials that are hard can consume a tool in a very short period of time and hence

the tool life is much more unpredictable. For experiments, we have chosen brass which is considered to be easily machinable.

Dependent variables:

Dependent variables are those that will change during the experiments and will be measured in the experiments

1. Chip count:

The chip count is the variable of interest for the TWM system. This variable is expected to change during experiments and will be measured at a defined sampling rate by the system. The sampling rate of the system at the decided belt speed is 2 seconds (0.9 seconds belt moving time + 1.1 seconds idle time).

State Variables:

1. Minimum feed: (F_{min})

This variable can neither be modified nor controlled, but is expected to change during the cutting process. The minimum feed is a critical state variable. It has a lower limit that has to be maintained at the start of every experiment due to the Minimum Chip thickness effect. This factor is dependent on the tool flutes (n), spindle speed (N) and the uncut chip thickness. The initial feedrate (independent variable) is selected based on this value. The minimum feed is F_{min} from the cutting edge radius r_e using Eqn. (8).

$$F_{min} = 0.3 \times r_e \tag{8}$$

2. Cutting edge radius: (r_e)

The cutting edge radius of the tool depends on and varies with changing tool condition. This is measured 'offline' using an optical microscope before and after the

cutting operation. The cutting edge radii for new tools have some variability from tool to tool. The two cutting teeth of the same tool can also be slightly different.

All the process parameters and their values are summarized in Table 2.

Table 2: Parameter values for the experiments

Parameter (Symbol)	**Values / Description**
Spindle speed, (N)	80,000 rpm
Axial depth of cut (z)	40 µm
Tool diameter (D)	200 µm
No. of teeth (n)	2
Min. Feed (Depends on cutting edge radius)	1.6 mm/s (Assuming 2 µm edge radius)
Belt speed (V)	139 mm/s
Air supply pressure (P)	100-40 Psi
Workpiece material	Brass

4.2 EXPERIMENTAL DESIGN

In order to evaluate the hypothesis, micromilling cutting needs to take place in two conditions: above and below the minimum chip thickness. Two sets of experiments were designed. The system variables are kept constant for these experiments, and independent variables are varied.

4.2.1 Type-1 experiment

The Type-1 experiment has been designed to be a multi-level single factor experiment. The feedrate and the cutting time are both varied. The cutting edge radius of the new tool is first measured as shown in Figure 28, and using Eqn. (1), the minimum feedrate is calculated. Five levels of feedrate are chosen. This will give information over a large range of feedrates and will make the results more significant. The rest of the process variables are held constant. The feeds and corresponding feedrates are shown in Table 3.

Table 3: The feeds and feedrates selected for all Type-1 experiments.

	Pass 1	Pass 2	Pass 3	Pass 4	Pass 5
Feed per tooth (µm/tooth)	1.2	1.0	0.8	0.6	0.4
Feedrate (mm/s)	3.2	2.67	2.13	1.6	1.06

During the cutting experiment, the tool wear increases as the cutting time increases and hence the cutting edge radius is expected to change continuously. Each cutting run would have to be done using a new cutting tool in order to negate this effect. However, doing so would increase the cost of experiments, and could induce random error due to a variation in tool construction, mounting, process etc. Experience shows that the since the workpiece material is brass, rapid tool wear is not expected as it is a comparatively soft material. This allows the assumption that the cutting edge radius is not significantly decreased for the six experimental runs.

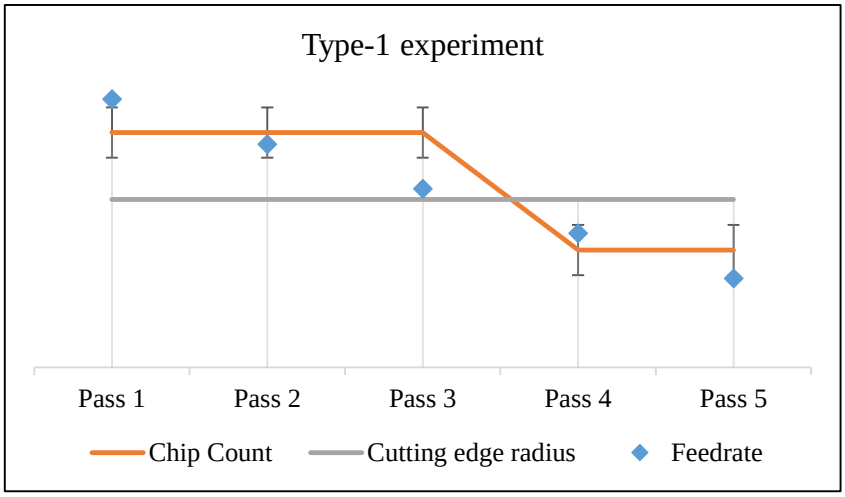

Figure 26: Illustration of hypothetical Type-1 experiment results

The expected graph of results for the experiment is illustrated in Figure 26. From Pass 4 onwards, the feedrate will be below the theoretical minimum chip thickness and hence the chip count is expected to drop after that pass. The experiment

will provide a relation between chip count and feedrate. This will help evaluate the mathematical relationship between the feedrate and minimum chip thickness. Some variance is expected in the values of the chip count, which is illustrated with error bars.

4.2.2 Type-2 experiment

The Type-2 experiment is designed by keeping the feedrate constant and increasing the cutting time. The cutting tool will cut parallel linear paths of equal cutting length for a long period of time. The chip count is recorded continuously during cutting and cutting is continued until a drop in the chip count is observed. At this point, the cutting is stopped and the cutting edge radius will be recorded.

The expected graph of results for the experiment is illustrated in Figure 27. This experiment will provide a relation between chip count and cutting time. This will help evaluate the hypothesis by checking whether or not the cutting was taking place above or below the MCT threshold. Once again, some variance is expected in the values of the chip count, which is also illustrated with error bars. The cutting edge radius increase might not be linear.

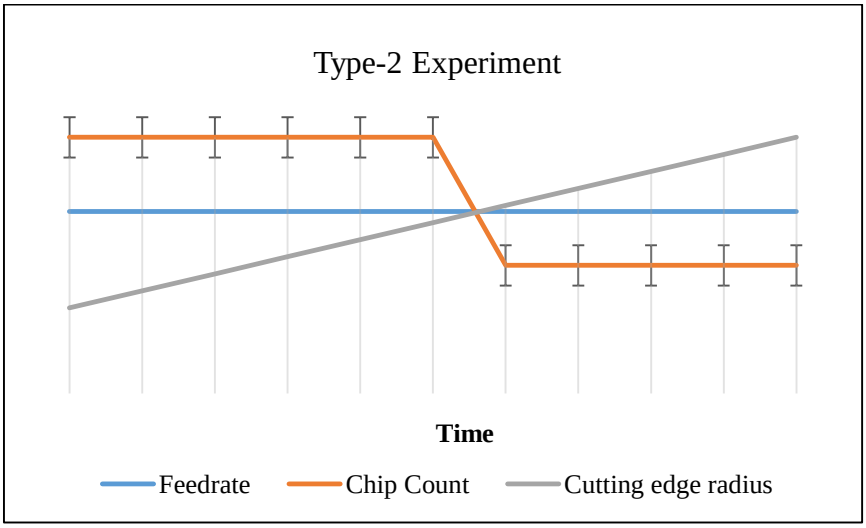

Figure 27: Illustration of hypothetical Type-2 experiment results

To evaluate the success of the system in getting a correct chip count, the expected number of chips per frame captured is calculated. This depends on the spindle speed of the cutting tool which defines the number of chips produced, the field of view of the camera which defines the area captured, and the belt speed which defines the number of chips per area. The belt speed is chosen to be 139 mm/s. By using Eqns. (2), (4) and (5), calculation is performed as given below:

- Number of chips produced per second (hypothesized) = 2,666
- Field of view of camera in the belt motion direction = 31.75 mm
- Speed of the belt = 139 mm/s
- Chips expected per frame = (2666/139) *31.75 ≈ 600

The image needs to be cropped due to unequal focus across the field of view; the edges of the image are out of focus when the center of the image is in focus. It is assumed that the chip distribution will be more or less even across the image. The area cropped reduces the total field of view by 420 pixels in the x direction and 300 pixels in the y direction. Therefore, the analyzed area of each image is reduced to approximately 52%. Based on this, the expected chip count per frame for both the experiments will be approximately 310.

4.3 EXPERIMENT EQUIPMENT AND PROCEDURE

The following is a list of equipment and external apparatus used for the experimental evaluation of the hypothesis. The procedure for performing the experiment follows.

1. Machine-Tool: The cutting tests are performed on a micro/meso scale precision cutting machine tool. The machine uses Beckhoff CPU, drivers and servo-motors.

The software used to interface with the machine was TwinCAT3, which is a Visual Studio integrated software which allows for PC-based real-time control of the machine. A PC-based control allows for future integration of applications such as Matlab and LabView into the system.

2. Tool observation microscope: The new cutting tools are observed under the Nikon MA100 inverted optical microscope. This microscope can capture digital images of the tool and allow measurement of the cutting edge radius of the tool. Figure 28 shows a picture of the tool from the bottom and the measurement of its cutting edge radius.

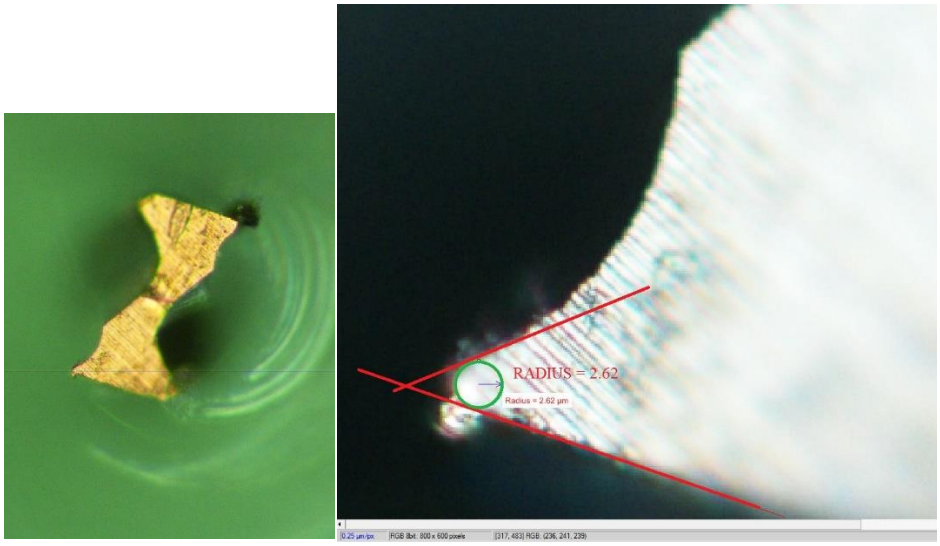

Figure 28: (L to R) A picture of the micro endmill, and the measurement of the cutting edge radius

Procedure:

1. The Machine-Tool is switched on and the 200 µm tool is inserted into the spindle. This spindle is brought to its home position, which is slightly above the workpiece to allow for tool touch-off.
2. The sub-systems of the TWM system are switched on. Power supply to the lighting system, the motion and adhesion system is turned on and the PSoC and USB

microscope are initialized on a PC. Power to the PSoC is turned off, which causes the belt to remain stationary, which otherwise would start consuming the adhesive tape.

3. The air-supply to the suction pump is turned on. This also supplies the air to the spindle of the machine-tool.
4. Tool registration is performed by slowly plunging the tool into the workpiece till electrical continuity is obtained upon touch-off. The desired axial depth of cut is set and the tool is in a ready position.
5. The PSoC power is turned on, and the cutting is simultaneously started. The system runs automatically. After the channel is fully cut, the belt is stopped and the image data that is recorded is saved. The used adhesive tape is discarded, and the tool is brought to its next ready-position. The procedure is repeated for the required runs.

5 EXPERIMENTAL RESULTS AND ANALYISIS

This Chapter describes the results from the experiments and their analysis. Section 5.1 shows the results of the first set of experiments performed. Section 5.2 describes the investigation of the variance in the data obtained from these experiments. Section 5.3 presents the results and analysis of the final experiment performed and the analysis of the data obtained.

5.1 FIRST SET OF EXPERIMENTS

The first set of experiments consists of two experiments: A Type-1 experiment, in which both feedrate and cutting time are independent variables, followed by a Type-2 experiment, in which cutting time is the only independent variable.

5.1.1 Type-1 experiment

Table 4 shows the raw data obtained from the Type-1 experiment. The missing readings in this experiment are due to a shorter cutting time in the first three feedrates. The faster feedrates lead to lower number of captured images per cutting tool pass. Therefore, the data collection i.e. number of images in the slower feedrates was restricted to have the same number of observations as the faster feedrates.

Table 4: Chip counts for experiment Type-1

Feed Rates	3.2 mm/s	2.67 mm/s	2.13 mm/s	1.6 mm/s	1.06 mm/s
Count 1	224	193	333	290	124
Count 2	236	227	282	232	206
Count 3	201	248	278	273	147
Count 4	230	205	295	289	195
Count 5	-	-	-	253	168
Mean	222.75	218.25	297	267.4	168
Std Dev	15.3	24.32	25.07	24.84	33.72

A box-plot shown in Figure 29 represents the data from the Type-1 experiment. The whiskers represent the maximum and minimum observed values; the orange blocks represent the range from the 25th to the 50th percentile, and the green block represents the 50th to 75th percentile.

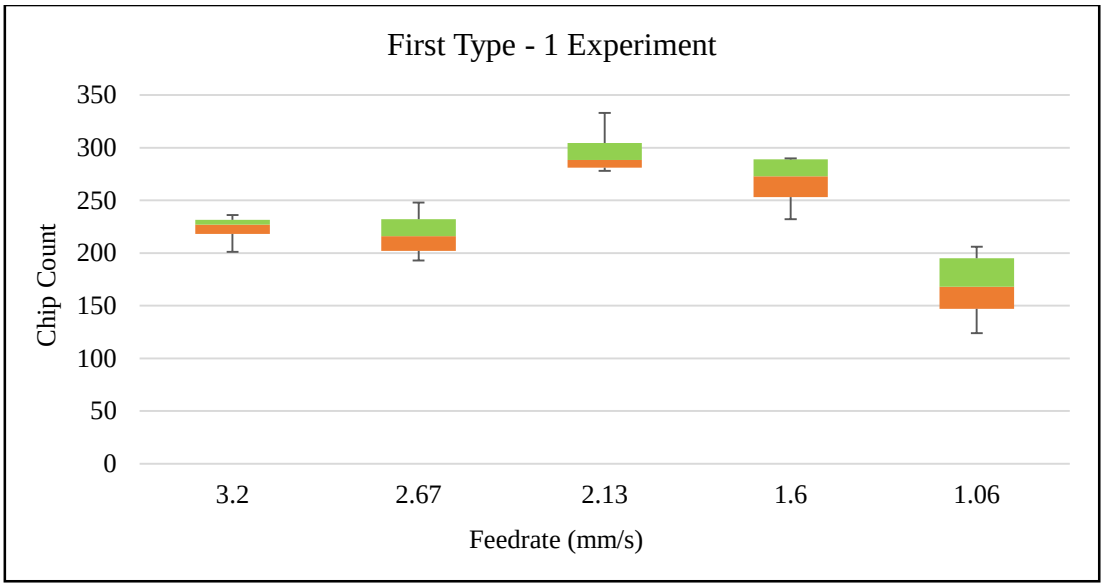

Figure 29: Box plot for the first Type-1 experiment

A single-factor ANOVA analysis is used to analyze the data. This will help determine whether or not the chip counts obtained by using the different levels of feedrate have a statistically significant difference. The null hypothesis is that the chip count averages for these treatments are equal; the alternate hypothesis is that the chip count averages are significantly different, as shown in Eqn. (9).

$$H_0: \mu_1 = \mu_2 = \mu_3 = \mu_4 = \mu_5$$
$$H_1: \mu_1 \neq \mu_2 \neq \mu_3 \neq \mu_4 \neq \mu_5 \quad (9)$$

The results of the ANOVA are shown in Table 5.

At ($\alpha = 0.05$) 95% confidence, the F_{crit} value is 2.964, meaning that there is a statistically significant difference in the chip count caused by the different feedrates.

The ANOVA robustness tests such as the normal probability plot and plot of residuals over time, are shown in the Appendix D.

Table 5: Single-factor ANOVA for type-1 experiment

Source of Variation	SS	DOF	MS	F	P-value
Between Feedrate	44715.89	4	11178.97	16.695	1.01E-05
Error (Within Feedrate)	11382.7	17	669.5706		
Total	56098.59	21			

A contrast test is then performed in order to evaluate the data with a more realistic null hypothesis. Since it is known that the two runs with the highest feedrates take place above the theoretical minimum chip thickness and that the runs with the lowest two feedrates take place below the theoretical minimum chip thickness, a comparative t-test can be performed to find significant difference between the feedrates above the minimum chip thickness and the feedrates below the minimum chip thickness, if any. The null and alternate hypotheses are given in Eq. (), where μ_i is the mean for the i^{th} feedrate level

$$H_0: \mu_1 + \mu_2 = \mu_4 + \mu_5$$
$$H_1: \mu_1 + \mu_2 \neq \mu_4 + \mu_5 \quad (10)$$

Contrasts are coefficients to these means; in this case the contrasts are: c1, c2 = +1; c3 = 0; c4, c5 = -1.

The contrast of interest can be written as:

$$C = c_1\mu_1 + c_2\mu_2 - c_4\mu_4 - c_5\mu_5 \quad (11)$$

The variance for C is:

$$V(C) = \frac{\sigma^2}{n}\sum_{1}^{5} C_i^2 \quad (12)$$

Then the value t_0 is calculated as:

$$t_0 = \frac{C}{V(C)} \tag{13}$$

The value of t_0 obtained for the data in Table 4 is 0.254. The t-critical value at 95% confidence is 1.74. This means that we fail to reject the null hypothesis, meaning that for the comparison of interest, there is *no significant difference* in the chip count when cutting above or below the theoretical MCT.

5.1.2 Type-2 Experiment

Table 6 shows the raw data of the type-2 experiment. The process parameters used for micromilling were the same as shown in Chapter 4. The two missing readings in Table 6 are due to extremely inferior quality of image in those cases. A time-series plot, as shown in Figure 30 represents the data from the Type-2 experiment. A moving average of the fourth interval is used to observe any trends seen in the data. The descriptive statistics are given in Table 7.

Table 6: Chip counts obtained for experiment Type-2

Pass	**1**	**2**	**3**	**4**	**5**	**6**	**7**	**8**	**9**	**10**	**11**
Count 1	175	220	199	199	169	213	283	242	237	239	243
Count 2	302	205	286	200	188	321	258	299	201	278	304
Count 3	227	195	269	158	199	281	188	206	213	314	346
Count 4	262	149	230	190	207	306	181	347	285	331	246
Count 5	191	191	-	161	299	-	292	282	366	196	351

Table 7: Descriptive statistics for Type-2 experiment

Chip Count	**Mean**	**Std Dev**	**Median**	**Range**	**Min**	**Max**
Raw	243.77	57.08	237	317	149	366
Moving average (Int=4)	242.16	38.5	245.75	142.25	169.5	311.75

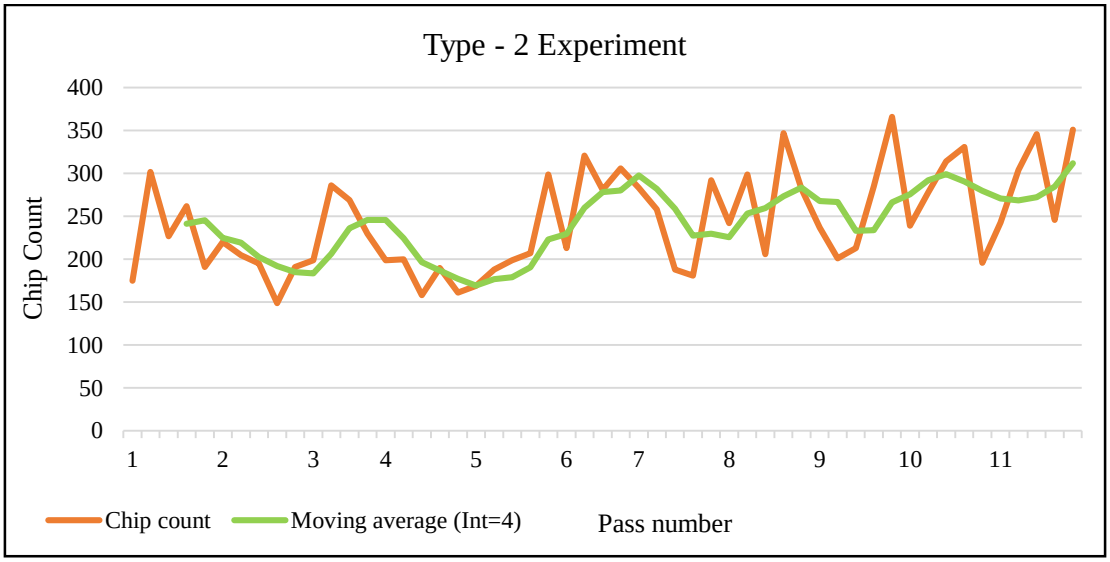

Figure 30: Time/Pass vs Chip count plot of the Type-2 experiment

What is observed here is a large standard deviation in the observed chip count. This is seen over the range of the experiment, as the standard deviation for the raw data is as high as 57, when the means is 243. The chip count in this experiment has not dropped; in fact, it shows a slight upward trend. Even if the chip count were to fall to half the number, it would be hard to distinguish between the two sets of data due to the large standard deviation.

This variance is also observed between succeeding values within the same pass, or consecutive passes. For instance, the minimum chip count of 149 appears in Pass 2, and a larger number of 286 is seen in Pass 3. A moving average of the fourth interval is used to detect any trends in the data. The plot shows a continuously varying chip count and fails to reveal the expected trend in the data.

In both the experiments, the data appears to contradict the expected trend in chip count described in Chapter 4. However, it is difficult to draw a conclusion in regard of

the chip production and the underlying cutting mechanics due to such a large variance in the data. The variance can also be caused due to errors caused by some operating parameters set in the TWM system. Therefore, experiments are performed in order to investigative the variance before performing any hypothesis evaluation experiments. These are described in the next section.

5.2 INVESTIGATING THE VARIANCE

The investigation of the data first focused on the variance that could be potentially caused by the TWM system itself. Some possible reasons are identified below, and a designed experiment was performed to analyze the variance.

- The metal chips could get stuck or clogged in the chip suction system, which can be later dislodged onto the adhesive tape, causing ejection of chips at an erratic rate. In order to reduce this possibility, the travel distance or 'length of the inlet tube' need to be shortened. This impact of this variable would be tested by employing the originally used long inlet tubing (0.9 m) and using a shorter tube (0.45 m).
- The medium of transport for the metal chips is air. The suction force for the vacuum pump is generated by compressed air. There is a possibility that the air flow in the system is turbulent, which causes the metal chips to travel at uneven rates. This is tested as a separate experiment to analyze the air flow out from the pump, which is named "*Variance test-1*".
- The chips could be exiting the system at a very high velocity from the nozzle. This could possibly cause an unknown and varying amount of chips to be lost. The variable that would be tested is the 'Supply pressure' into the pump, by using a lower supply pressure which would lower the vacuum flow in the pump.

- The last factor taken into consideration is the length of the workpiece. The original workpiece is short compared to the size of the hood. This might cause an improper suction closure for large parts of the cutting operation. A longer workpiece could be used to investigate this potential source of variance. A longer workpiece would also provide a larger set of readings. The short workpiece is 1 inch in length, and the long workpiece will be 4 inches in length

5.2.1 Variance test 1: Air flow

Two of the critical factors that are under question relate to the possibility of air flow fluctuations and the high air exit velocity. To analyze this, the vacuum pump is connected to an air flow sensor. Pressurized air is supplied to the pump at different pressures and the readings obtained from the sensor are recorded using an oscilloscope. The test is performed at 100 psi, 50 psi, 40 psi, 30 psi, 20 psi and 10 psi.

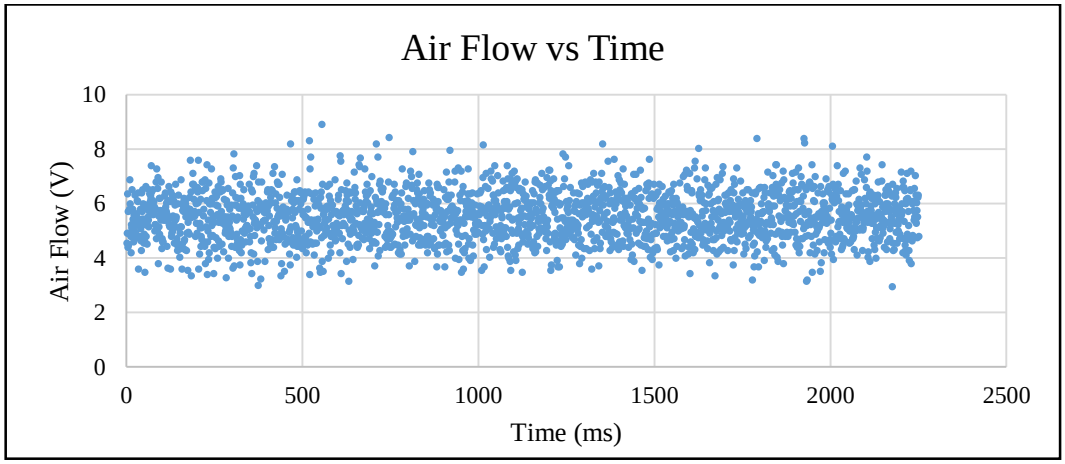

Figure 31: The scatter plot for air speed readings in time (50 psi)

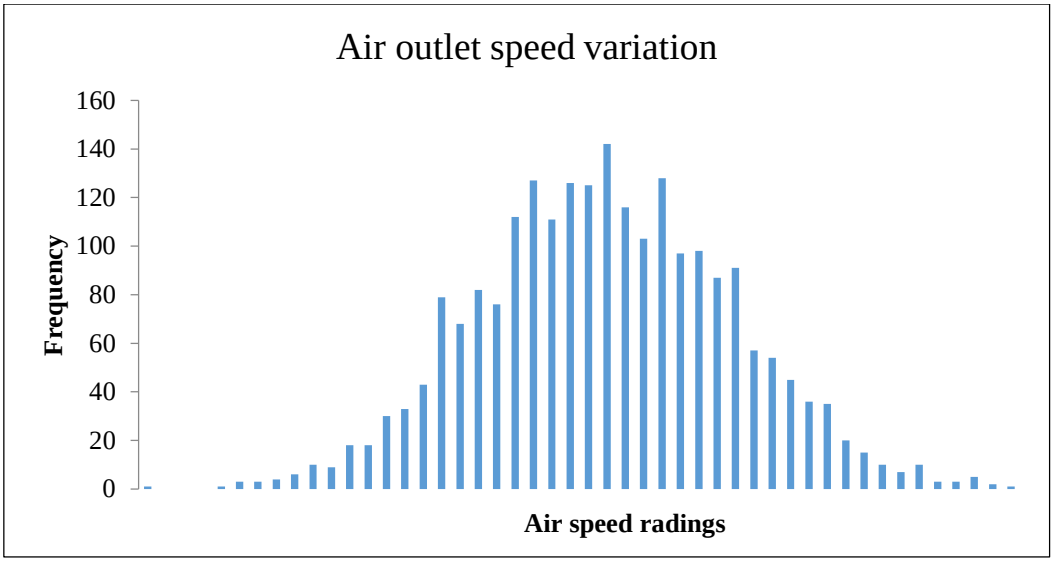

Figure 32: A histogram plot showing the dominant air flow reading (50 psi)

Figure 31 shows the data obtained from the air flow sensor for the test performed at 50 psi. Similar results are obtained for the other inlet pressure tests. Figure 32 shows a histogram which gives an idea of the distribution of the air flow values obtained. We see a normal distribution with a large variance in the air flow. This can be expected if the air flow is turbulent in nature. To analyze whether or not the air speed variation is the cause of the variation seen in the chip count, statistical analysis is done.

Statistical analysis:

The sampling rate of the air flow sensor is 2 milliseconds. This sampling rate is much higher compared to the time it takes the tape to travel the distance of one image FOV, which is 31.75mm. At the given belt speed, it would take the tape 220 milliseconds to travel the distance FOV_x. Therefore, the data is grouped into time intervals of 220 milliseconds. The variance and mean within each of these groups is calculated. Finally, a pooled variance is calculated to obtain the value for the mean air flow and variance which affects every succeeding images. Table 8 summarizes that data.

Table 8: Results of descriptive statistics for the air flow tests

Air flow (psi)	100	50	40	30	20	10
Pooled mean (V)	8.046	5.966	5.97	5.851	5.526	4.606
Pooled Std Dev (V)	1.48	1.11	0.95	0.88	0.87	0.61

The data shows a proportionally steady rise in the exit air flow reading and the variance associated with it with respect to the input supply pressure. However, what is also revealed by the data is that the mean air flow reading for each picture time is similar and has very little variance among those values. This is illustrated in Table 9, where a list of the mean airflow over a picture time is shown. This data proves that despite varying, the air flow over a 'picture time' (220 ms) remains the same. Hence, the variation would be within pictures and not between pictures. This shows that the variance in the air flow happens at a much higher frequency than the frequency of variation of the number of chips seen in the experiment results between pictures.

Table 9: Table showing the mean airflow over a 'Picture-time' (20 psi)

Picture #	1	2	3	4	5	6	7	8	9	10
Mean	5.5	5.44	5.44	5.47	5.40	5.48	5.51	5.54	5.47	5.64
Picture #	**11**	**12**	**13**	**14**	**15**	**16**	**17**	**18**	**19**	**20**
Mean	5.59	5.57	5.49	5.64	5.53	5.53	5.51	5.54	5.6	5.55

5.2.2 Variance test-2: Designed experiment

After ruling out the effect of the air flow variation, a two-factor full-factorial experiment was designed to test the effect on chip number variance of the change in length of the workpiece and the length of the inlet tube. Table 10 shows the chip count data obtained.

Table 10: Chip count for the variance experiment

Run type	WP(L) / Tube(S)	WP(L) / Tube(L)	WP(S) / Tube(S)	WP(S) / Tube(L)
Count 1	228	221	368	206
Count 2	257	602	274	189
Count 3	489	279	135	141
Count 4	312	515	164	175
Count 5	351	493	158	130
Count 6	548	574	213	231
Count 7	469	701	230	351
Count 8	323	595	149	241
Count 9	424	233	182	285
Count 10	273	457	225	158
Mean	367.4	467	209.8	210.7
Std Dev	174.37	168.16	70.43	68.67
Q1	282.75	323.5	159.5	162.25
Median	337	504	197.5	197.5
Q3	457.75	589.75	228.75	238.5

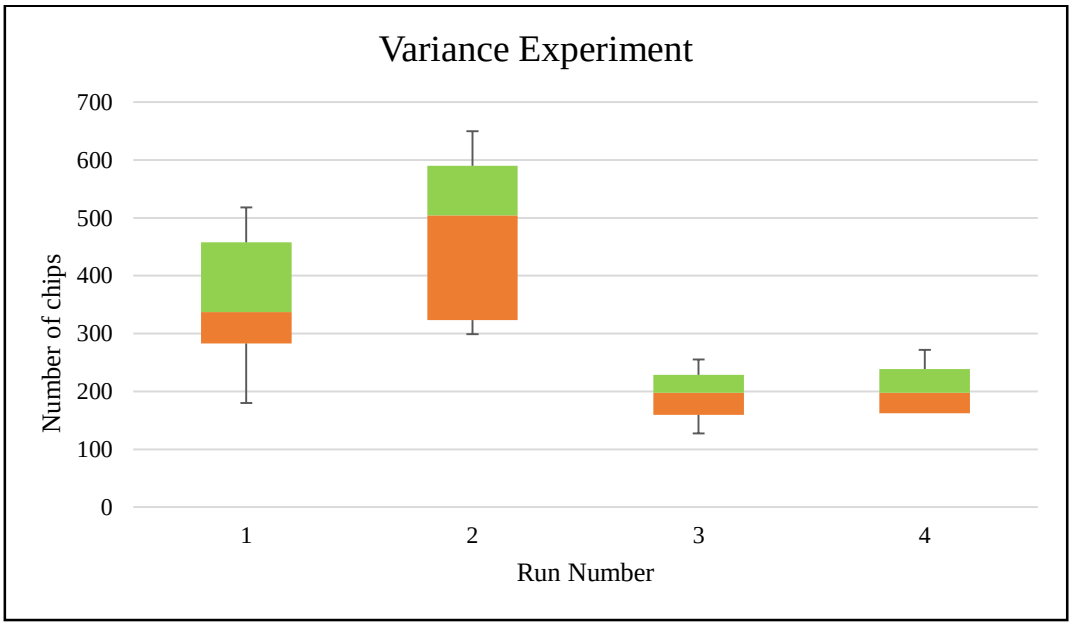

Figure 33: Box plot for the variance experiment data

Table 11 shows the ANOVA results on the data. The null and the alternate hypothesis are stated as shown in Eqn. (14), where τ is the error or variance caused by

the workpiece change and *ß* is the error or change due to the change in the tube, and *i* and *j* represent the row and column number.

Table 11: Two-factor ANOVA for the variance experiment

Source of Variation	SS	DOF	MS	F_0	P-value
Workpiece	428283	1	428283	34.38689	1.06E-06
Tube length	25250.62	1	25250.62	2.027375	0.163098
Interaction	24354.23	1	24354.23	1.955403	0.170561
Error	448374.1	36	12454.84		
Total	926262	39			

$$H_0: (\tau\beta)_{ij} = 0$$
$$H_1: at\ least\ one\ (\tau\beta)_{ij} \neq 0 \quad (14)$$

The F-critical value for this experiment is 4.1132. Upon comparing to the F_0 values, this means that a change in workpiece length has a significant effect on the value of chip count obtained. The length of the tube on the other hand, seems to have a very small effect on the final chip count.

Upon comparing the individual data, it is found that the run with the long workpiece and a short tube has a mean value much closer to the expected number of chips. The variance shows a trend of increasing with an increased mean.

The mean for the long workpiece & short tube is found to be closer to the expected chip count. From the air speed simulation, it was found that the variance in the flow is not responsible for the variance. However, using 40 psi supply pressure reduces the air speed at the exit. This would help reduce any loss of chips happening at the exit. Therefore, the final experiment that will be performed will use a long workpiece and a short tube with a 40 psi suction supply pressure.

5.3 FINAL EXPERIMENT

The final experiment performed was a Type-1 experiment (varying feedrate with increasing cutting time). Based on the variance experiment, it was determined that the experiment will be performed with a long workpiece, a short inlet tube and at 40 psi pressure. This experiment is expected to have a lower variance as compared to the previous experiments due to the reduced pressure.

The analysis of the data follows the same flow as the previous type-1 experiment. The raw data and the descriptive statistics are given in Table 12. An ANOVA is then performed on the data to quantify the effect of the changing feedrates. The null and alternate hypothesis for this test are the same as stated in Eqn. (9).

Table 12: Chip count for second Type-1 experiment

Feedrate (mm/s)	**3.2**	**2.67**	**2.13**	**1.6**	**1.06**
Count 1	207	228	197	162	211
Count 2	427	244	164	200	186
Count 3	378	377	182	147	219
Count 4	473	146	178	242	283
Count 5	269	249	260	167	186
Count 6	424	201	331	226	192
Count 7	377	172	323	247	141
Count 8	356	162	248	221	185
Count 9	146	358	319	275	162
Count 10	157	340	192	240	193
Mean	321.4	247.7	239.4	212.7	195.8
Std Dev	118.2	83.9	65.8	42.2	37.8
Q1	222.5	179.25	184.5	175.25	185.25
Median	366.5	236	222.5	223.5	189
Q3	412.5	317.25	304.25	241.5	275

A box plot for this data is shown in Figure 34 to visualize the data.

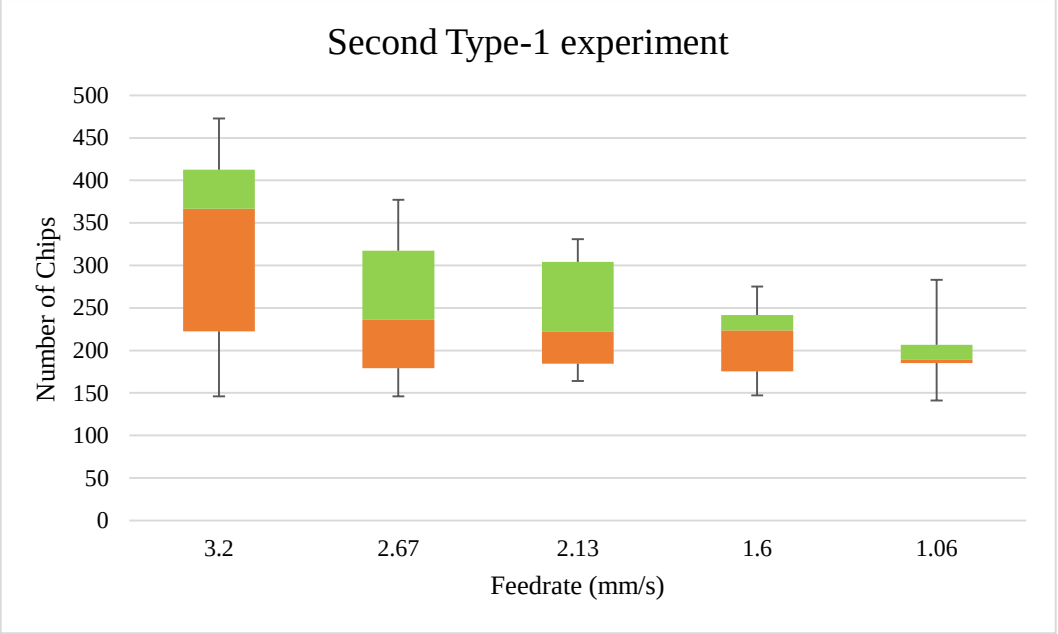

Figure 34: Box plot representation for the final experiment

Table 13: Single factor ANOVA Table of Type-2 experiment

Source of variation	SS	DOF	MS	F_0	P-value
Changing feedrate	93267.4	4	23316.9	4.0813	0.0066
Error (within treatments)	257087	45	5713.04		
Total	350354	49	7150.08		

The F-critical value, at 95% confidence for this test is 2.578. Since F_0 > F critical, it means that there is a statistically significant difference in the chip numbers caused by the changing feedrates.

Once again, a contrast test is performed on the data. Eqns. (11), (12) and (13) are used to perform the test. The null and alternate hypothesis are the same as in Eqn. (10).

The value of t_0 for this test was found to be 6.714. The t-critical value at 95% confidence for this test is 1.68. Therefore, t_0 > t-critical value for this test; which means that the cumulative data above and below the theoretical minimum chip thickness of the tool are *significantly different*.

However, when the means are compared directly, the drop in chips even though significant, is not close to being half. The drop in chips is approximately 70%. The implications of this result on the hypothesis is discussed in the next Chapter.

6 DISCUSSION AND CONCLUSION

This Chapter draws inferences from the work done in the thesis. Section 6.1 discusses the accomplishments of the thesis work as compared to the objectives that were undertaken at the start. Section 6.2 evaluates the hypothesis that was defined in the first Chapter and tries to draw meaningful conclusions from the data.

6.1 ACCOMPLISHMENT OF THE OBJECTIVES

The research work in this thesis addresses the problem of tool wear in micromilling. The work also hypothesizes, develops and analyses an online tool wear modeling system for micromilling.

Objective 1: To develop a prototype Online Tool Wear Modeling system that utilizes chip production rate as an indirect signature.

- A promising online TWM system has been developed that successfully counts chips without interrupting the micromilling process.
- Key sub-systems such as the Pneumatic sub-system and motion and adhesion systems have been developed, and new knowledge about the impact of their operating variables has been established.
- The image acquisition and processing sub-system has been developed and tested. A robust image processing algorithm and the sequence of operations have been established after multiple iterations.

Objective 2: To evaluate the effectiveness of the prototype device to measure chip production rate.

- Key governing equations for the system have been established as shown in Chapter 3.

- A variance analysis experiment was performed to evaluate the system. The knowledge obtained gave insight into the challenges faced and the future work required for the system.

Objective 3: To provide an empirical proof-of-concept for chip production rate as an indirect signature of tool wear.

- The data obtained makes it hard to draw decisive conclusions on the hypothesis.
- More experiments with multiple other factors will have to performed to establish a relationship between chip production rate and the tool wear.
- Better understanding of the mechanics of chip production, and the effects of machining parameters might be needed to evaluate the hypothesis. The final experiment showed that there is a difference between the chip numbers above and below the minimum chip thickness.

6.2 DISCUSSION ON THE DATA

The original primary hypothesis of this work was stated as follows:

"*During micromilling, if the cutting edge radius of the micro end mill wears so that the uncut chip thickness drops below the minimum chip thickness, the number of chips produced per unit time will drop by approximately half as compared to when the tool is new.*"

The final type-1 experiment showed a decrease in the average number of chips between the runs that were above and below the theoretical MCT. However, it also appears that the mean of the number of chips drops steadily with every stepped reduction in feedrate, regardless of the MCT threshold. The drop in the number of chips

is also not at around 50% of the initial readings which were taken with a new tool; the mean of the slower feedrates is around 70% of the runs above the MCT threshold.

Primary conclusions from each experiment are given in Table 14.

Table 14: A summary of the conclusions from the experiments

Experiment	Conclusions / Discussion
Type – 1 experiment (1)	The data does reveal a significant difference in chip number between the various levels of feedrate. However, the contrast test shows no difference despite cutting above and below the theoretical MCT.
Type – 2 experiment	The data reveals a large variance in consecutive readings of chip count. After cutting for a large number of passes, the chip count doesn't fall.
Variance experiment	The experiments and simulations reveal that a reduction in air supply pressure reduces the air exit velocity, while still providing sufficient suction. The length of the workpiece shows a significant effect on the mean chip count, whereas the length of the suction tube doesn't affect the outcome
Type – 1 experiment (2)	The data shows a significant difference between the various levels of feedrate. The contrast test also confirms a difference in the count between cutting above and below theoretical MCT.

However, a large variance is seen in the readings. There is also an overlap of the minimum and maximum values between runs where the expectation is that of a large gap between the readings. Various causes of the variance were investigated and identified, however, the final experiment reveals that some sources of variance still

remain. This makes it difficult to draw a decisive conclusion despite showing a statistically significant difference.

The next Chapter on future work discusses what measures can help identify and reduce the variance caused due to the TWM setup, and perform further experiments to re-evaluate the hypothesis

7 FUTURE WORK

The study done and the experimental efforts have revealed the requirement for additional experiments in order to obtain a better understanding of chip formation and thereby, an understanding of the process.

7.1 TOOL WEAR MODELING

In Chapter 1, the hypothesis proposed a relation of the minimum chip thickness requirement and the feedrate requirement of micromilling to the number of chips produced. Chapter 4 discussed the results that would be expected theoretically if this hypothesis was correct. However, the results obtained have seen large variation in the chip count obtained even in successive readings of the values. For experiment Type-2, the variance stays large enough which makes it difficult to draw a statistically significant conclusion. The Type-1 experiment shows a statistical difference between the various levels of federate. However, there was no sudden drop in the chip number as was expected. Further experimentation on the system variables are required to analyze the high variance in chip count. The second phase would involve a study of experiments with different workpiece materials and its effects.

- Offline experiment: This experiment hypothesizes the start-stop motion of the belt as the cause for the high variance obtained. The belt's acceleration time, deceleration time and the backlash of the belt can potentially lead to stationary areas of the tape being photographed. An experiment where the pictures are taken after the cutting test is complete will permit running the belt at a constant speed. Analyzing the data for this experiment can rule-out or establish this as a cause for the variance

- Filter experiment: This experiment hypothesizes a variable loss of chips at the exit nozzle as a cause for the high variance. This experiment will involve a much larger change in the setup. It hypothesizes the use of a moving filter material instead of a sticky tape which will capture all the chips. This will require extensive testing to check the image quality that is obtained from a variety of filter types. The image processing algorithm will have to be altered accordingly as a change in the background can lead to vastly different results.

If the results from the above experiments fail in explaining the variance, further study will be necessary in order to understand the chip formation mechanics in micromilling.

7.2 TOOL WEAR MEASUREMENTS

In Chapter 2, we have argued that the cutting edge radius is a better measure of tool wear in micromilling using current equipment such as optical microscopes or SEM microscopes. This process is done offline and to develop this TWM system further, an online system is needed. The current measurement methods of the cutting edge radius provide the measurement of the bottom view of the tool as seen in Chapter 5. The cutting edge of the tool extends along the entire profile of the tool. Another reason why the cutting edge radius is a better measure is because flank wear has a lot of ambiguity associated with it when the ‘wear land’ is measured. This can cause inconsistent measurements which are subject to human error. These measuring methods also require repeated removal of the tool from the spindle at various stages of machining and taking physical measurements.

A new method of measuring wear is being proposed. The requirement for obtaining reliable and repeatable measurements is ‘unrolling’ the cutting surface of the tool. This is possible by generating an impression of the flutes of the tool onto a cellulose acetate tape. This procedure requires the use of the precise axes of the machine tool and the frictionless bearings of the spindle; and hence can be automated. The common parameters of the tool such as the cutting edge radius can be extracted from the radius of curvature of the bottom of the trough and can be observed along the entire flute length. Flank wear can also be recorded by the impression produced by the flank surface while rolling the tool. In addition, other surface data such as crater wear can also be obtained.

8 REFERENCES

[1] S. Filiz, L. Xie, L. E. Weiss, and O. B. Ozdoganlar, "Micromilling of microbarbs for medical implants," *Int. J. Mach. Tools Manuf.*, vol. 48, no. 3–4, pp. 459–472, Mar. 2008.

[2] J. Li, C. R. Friedrich, and R. S. Keynton, "Design and fabrication of a miniaturized, integrated, high-frequency acoustical lens–transducer system," *J. Micromechanics Microengineering*, vol. 12, no. 3, p. 219, May 2002.

[3] V. Singh, Y. Desta, P. Datta, J. Guy, M. Clarke, D. L. Feedback, J. Weimert, and J. Goettert, "A hybrid approach for fabrication of polymeric BIOMEMS devices," *Microsyst. Technol.*, vol. 13, no. 3–4, pp. 369–377, Jun. 2006.

[4] T. Masuzawa, "State of the Art of Micromachining," *CIRP Ann. - Manuf. Technol.*, vol. 49, no. 2, pp. 473–488, 2000.

[5] J. Chae, S. S. Park, and T. Freiheit, "Investigation of micro-cutting operations," *Int. J. Mach. Tools Manuf.*, vol. 46, no. 3–4, pp. 313–332, 2006.

[6] G. L. Benavides, D. P. Adams, and P. Yang, "Meso-machining capabilities," *Sandia Natl. Lab. Albuq. N. M.*, vol. 87185, 2001.

[7] Y. Okazaki, N. Mishima, and K. Ashida, "Microfactory—Concept, History, and Developments," *J. Manuf. Sci. Eng.*, vol. 126, no. 4, p. 837, 2004.

[8] X. Liu, R. E. DeVor, S. G. Kapoor, and K. F. Ehmann, "The Mechanics of Machining at the Microscale: Assessment of the Current State of the Science," *J. Manuf. Sci. Eng.*, vol. 126, no. 4, p. 666, 2004.

[9] E. Oberg, C. J. McCauley, and Knovel (Firm), *Machinery's handbook: a reference book for the mechanical engineer, designer, manufacturing engineer, draftsman, toolmaker, and machinist*, 28th ed. New York: Industrial Press, 2008.

[10] C.-J. Kim, J. R. Mayor, and J. Ni, "A Static Model of Chip Formation in Microscale Milling," *J. Manuf. Sci. Eng.*, vol. 126, no. 4, pp. 710–718, Feb. 2005.

[11] J. Wang, Y. Gong, G. Abba, J. F. Antoine, and J. Shi, "Chip formation analysis in micromilling operation," *Int. J. Adv. Manuf. Technol.*, vol. 45, no. 5–6, pp. 430–447, Mar. 2009.

[12] M. E. Merchant, "Mechanics of the Metal Cutting Process. I. Orthogonal Cutting and a Type 2 Chip," *J. Appl. Phys.*, vol. 16, no. 5, pp. 267–275, Apr. 2004.

[13] M. E. Merchant, "Mechanics of the Metal Cutting Process. II. Plasticity Conditions in Orthogonal Cutting," *J. Appl. Phys.*, vol. 16, no. 6, pp. 318–324, Apr. 2004.

[14] M. P. Vogler, R. E. DeVor, and S. G. Kapoor, “Microstructure-Level Force Prediction Model for Micro-milling of Multi-Phase Materials,” *J. Manuf. Sci. Eng.*, vol. 125, no. 2, p. 202, 2003.

[15] M. P. Vogler, S. G. Kapoor, and R. E. DeVor, “On the Modeling and Analysis of Machining Performance in Micro-Endmilling, Part II: Cutting Force Prediction,” *J. Manuf. Sci. Eng.*, vol. 126, no. 4, p. 695, 2004.

[16] A. Aramcharoen and P. T. Mativenga, “Size effect and tool geometry in micromilling of tool steel,” *Precis. Eng.*, vol. 33, no. 4, pp. 402–407, Oct. 2009.

[17] N. Ikawa, S. Shimada, and H. Tanaka, “Minimum thickness of cut in micromachining,” *Nanotechnology*, vol. 3, no. 1, p. 6, Jan. 1992.

[18] J.-D. Kim and D. S. Kim, “Theoretical analysis of micro-cutting characteristics in ultra-precision machining,” *J. Mater. Process. Technol.*, vol. 49, no. 3–4, pp. 387–398, Feb. 1995.

[19] M. A. Davies, Y. Chou, and C. J. Evans, “On Chip Morphology, Tool Wear and Cutting Mechanics in Finish Hard Turning,” *CIRP Ann. - Manuf. Technol.*, vol. 45, no. 1, pp. 77–82, 1996.

[20] Z. J. Yuan, M. Zhou, and S. Dong, “Effect of diamond tool sharpness on minimum cutting thickness and cutting surface integrity in ultraprecision machining,” *J. Mater. Process. Technol.*, vol. 62, no. 4, pp. 327–330, Dec. 1996.

[21] J. Macedo, K. Colvin, and D. Waldorf, “Machine vision course for manufacturing engineering undergraduate students,” *J. Manuf. Syst.*, vol. 24, no. 3, pp. 256–265, 2005.

[22] H. Golnabi and A. Asadpour, “Design and application of industrial machine vision systems,” *Robot. Comput.-Integr. Manuf.*, vol. 23, no. 6, pp. 630–637, Dec. 2007.

[23] S. Kurada and C. Bradley, “A review of machine vision sensors for tool condition monitoring,” *Comput. Ind.*, vol. 34, no. 1, pp. 55–72, Oct. 1997.

[24] K. Maekawa, T. Obikawa, Y. Yamane, and T. H. C. Childs, *Metal Machining: Theory and Applications*, 1st edition. London : New York: Butterworth-Heinemann, 2000.

[25] K. Zhu, Y. S. Wong, and G. S. Hong, “Multi-category micro-milling tool wear monitoring with continuous hidden Markov models,” *Mech. Syst. Signal Process.*, vol. 23, no. 2, pp. 547–560, Feb. 2009.

[26] I. Tansel, O. Rodriguez, M. Trujillo, E. Paz, and W. Li, “Micro-end-milling—I. Wear and breakage,” *Int. J. Mach. Tools Manuf.*, vol. 38, no. 12, pp. 1419–1436, Dec. 1998.

[27] P. Li, J. a. J. Oosterling, A. M. Hoogstrate, H. H. Langen, and R. H. M. Schmidt, "Design of micro square endmills for hard milling applications," *Int. J. Adv. Manuf. Technol.*, vol. 57, no. 9–12, pp. 859–870, Dec. 2011.

[28] M. Malekian, S. S. Park, and M. B. G. Jun, "Tool wear monitoring of micro-milling operations," *J. Mater. Process. Technol.*, vol. 209, no. 10, pp. 4903–4914, 2009.

[29] K. Jemielniak and P. J. Arrazola, "Application of AE and cutting force signals in tool condition monitoring in micro-milling," *CIRP J. Manuf. Sci. Technol.*, vol. 1, no. 2, pp. 97–102, 2008.

[30] K. Jemielniak, S. Bombiński, and P. X. Aristimuno, "Tool condition monitoring in micromilling based on hierarchical integration of signal measures," *CIRP Ann. - Manuf. Technol.*, vol. 57, no. 1, pp. 121–124, 2008.

[31] C.-L. Yen, M.-C. Lu, and J.-L. Chen, "Applying the self-organization feature map (SOM) algorithm to AE-based tool wear monitoring in micro-cutting," *Mech. Syst. Signal Process.*, vol. 34, no. 1–2, pp. 353–366, Jan. 2013.

[32] C.-L. Yen, M.-C. Lu, and J.-L. Chen, "Study of AE signal for tool wear monitoring in micro milling based on LVQ algorithm," in *13th International Symposium on Advances in Abrasive Technology, ISAAT2010, September 19, 2010 - September 22, 2010*, 2010, vol. 126–128, pp. 719–725.

[33] Q. Ren, M. Balazinski, L. Baron, K. Jemielniak, R. Botez, and S. Achiche, "Type-2 fuzzy tool condition monitoring system based on acoustic emission in micromilling," *Inf. Sci.*, vol. 255, pp. 121–134, Jan. 2014.

[34] M. Prakash and M. Kanthababu, "In-process tool condition monitoring using acoustic emission sensor in microendmilling," *Mach. Sci. Technol.*, vol. 17, no. 2, pp. 209–227, 2013.

[35] M.-C. Lu and B.-S. Wan, "Study of high-frequency sound signals for tool wear monitoring in micromilling," *Int. J. Adv. Manuf. Technol.*, vol. 66, no. 9–12, pp. 1785–1792, 2013.

[36] C.-W. Hung and M.-C. Lu, "Model development for tool wear effect on AE signal generation in micromilling," *Int. J. Adv. Manuf. Technol.*, vol. 66, no. 9–12, pp. 1845–1858, Jun. 2013.

[37] I. Tansel, M. Trujillo, A. Nedbouyan, C. Velez, W.-Y. Bao, T. T. Arkan, and B. Tansel, "Micro-end-milling—III. Wear estimation and tool breakage detection using acoustic emission signals," *Int. J. Mach. Tools Manuf.*, vol. 38, no. 12, pp. 1449–1466, Dec. 1998.

[38] I. S. Kang, J. S. Kim, and Y. W. Seo, "Cutting force model considering tool edge geometry for micro end milling process," *J. Mech. Sci. Technol.*, vol. 22, no. 2, pp. 293–299, Feb. 2008.

[39] Z. Kunpeng, H. G. Soon, and W. Y. San, “Multiscale Singularity Analysis of Cutting Forces for Micromilling Tool-Wear Monitoring,” *IEEE Trans. Ind. Electron.*, vol. 58, no. 6, pp. 2512–2521, Jun. 2011.

[40] I. N. Tansel, T. T. Arkan, W. Y. Bao, N. Mahendrakar, B. Shisler, D. Smith, and M. McCool, “Tool wear estimation in micro-machining.: Part I: tool usage–cutting force relationship,” *Int. J. Mach. Tools Manuf.*, vol. 40, no. 4, pp. 599–608, Mar. 2000.

[41] I. N. Tansel, T. T. Arkan, W. Y. Bao, N. Mahendrakar, B. Shisler, D. Smith, and M. McCool, “Tool wear estimation in micro-machining.: Part II: neural-network-based periodic inspector for non-metals,” *Int. J. Mach. Tools Manuf.*, vol. 40, no. 4, pp. 609–620, Mar. 2000.

[42] M. Kumar, S. N. Melkote, and R. M’Saoubi, “Wear behavior of coated tools in laser assisted micro-milling of hardened steel,” *Wear*, vol. 296, pp. 510–518, 2012.

[43] K. Hamaguchi, Y. Kagata, H. Shizuka, and K. Okuda, “Effect of tool tilting angle on tool wear and surface roughness in micro ball end milling,” *Adv. Mater. Res.*, vol. 325, pp. 606–11, 2011.

[44] A. SODEMANN, A. K. BAJAJ, and J. R. VAUGHN, “Systems and methods for real-time monitoring of micromilling tool wear,” WO2015120293 A1, 13-Aug-2015.

[45] F. Z. Fang, H. Wu, X. D. Liu, Y. C. Liu, and S. T. Ng, “Tool geometry study in micromachining,” *J. Micromechanics Microengineering*, vol. 13, no. 5, p. 726, Sep. 2003.

APPENDIX A

PERFORMANCE GRAPHS FOR VACCON DF 1-3 PUMP

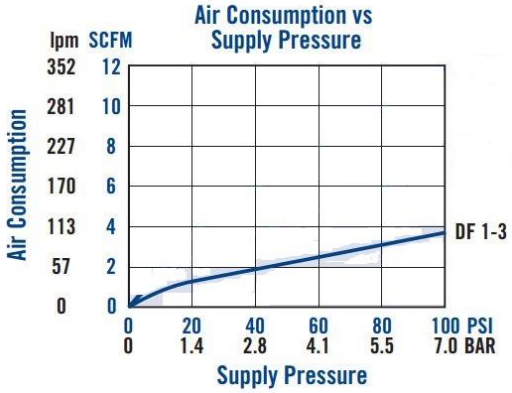
Air Consumption vs Supply Pressure
lpm SCFM
352 12
281 10
227 8
170 6
113 4
57 2
0 0
Air Consumption
DF 1-3
0 20 40 60 80 100 PSI
0 1.4 2.8 4.1 5.5 7.0 BAR
Supply Pressure

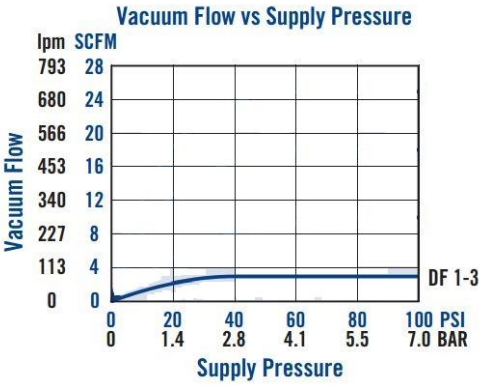
Vacuum Flow vs Supply Pressure
lpm SCFM
793 28
680 24
566 20
453 16
340 12
227 8
113 4
0 0
Vacuum Flow
DF 1-3
0 20 40 60 80 100 PSI
0 1.4 2.8 4.1 5.5 7.0 BAR
Supply Pressure

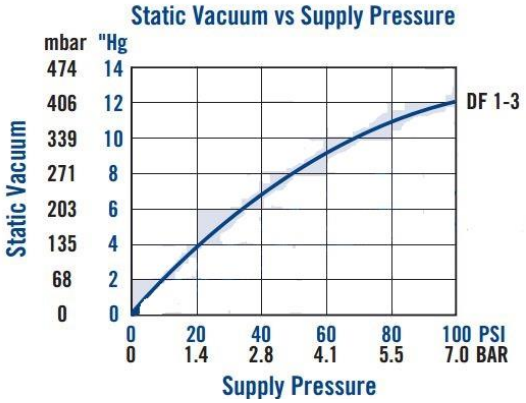
Static Vacuum vs Supply Pressure
mbar "Hg
474 14
406 12
339 10
271 8
203 6
135 4
68 2
0 0
Static Vacuum
DF 1-3
0 20 40 60 80 100 PSI
0 1.4 2.8 4.1 5.5 7.0 BAR
Supply Pressure

APPENDIX B

ALGORITHM FOR OPERATION OF THE MOTION SYSTEM

The following algorithm is used for the control of the two motors of the motion and adhesion sub-system

```
#include <project.h>
int main()
{
    // Define the ON-time based on distance between the
nozzle and the microscope and speed
    int Drive_Time=800;
    // Define the OFF-time based on time taken for the
belt to stop fully and the image capture time
    int Picture_Time=1200;
    int Drive_Speed=100;
    // Define variable to be sent as a Image trigger
    uint8 send=2;
    Tape_Roll_Motor_Start();
    UART_1_Start();
    Conveyor_Motor_Start();
    for(;;)
    {
      // Define speeds for the conveyor and tape roll
motor
      Conveyor_Motor_WriteCompare(20);
      Tape_Roll_Motor_WriteCompare(91);
      CyDelay(Drive_Time);
      // Send the image trigger
      UART_1_UartPutChar(send);
      // Stop the belt and the tape roll motor
      Conveyor_Motor_WriteCompare(0);
      Tape_Roll_Motor_WriteCompare(0);
      // Wait for the picture to be taken
      CyDelay(Picture_Time);
    }
}

/* [] END OF FILE */
```

APPENDIX C

MATLAB SCRIPT FOR IMAGING SYSTEM

The following MATLAB Script is used for the imaging sub-system

```
clear all
clc
%Generate a video object using the USB microscope%
vid=videoinput('winvideo',1,'RGB24_1280x1024');
%Start infinite frame acquisition allowing long standby%
set(vid,'TriggerRepeat',Inf);
%Start video - USB microscope%
start(vid);
%Define communication port to PSoC%
SerPSoC=serial('COM3');
set(SerPSoC,'BaudRate',9600,'DataBits',8,'Parity','none',
'StopBits',1,'FlowControl','none');
%Open communication with PSoC%
fopen(SerPSoC);
%Pre-define structuring element for image processing%
Se = strel('square',2);
%Define loop variables%
i=1;
a=0;
while (i<11) %Number depends on number of frames needed
per run%
  while (a==0)
      %Wait for non-zero value (trigger)%
      a=fread(SerPSoC,1,'uint8');
  end
  %Trigger has been received, so take a picture%
   a=fread(SerPSoC,1,'uint8');
   %Pause for belt to come to a complete halt%
   pause(0.5);
   %Take picture%
   data=getdata(vid,1);
   %Save picture for future reference%
   figure;imshow(data)
   B = rgb2gray(data); %Convert to grayscale%
   B(B>160)=0; %Blacken lusturous chips%
   %Crop image to obtain ROI%
   B2 = imcrop(B,[140,140,850,700]);
   B2(B2<130)=0; %Blacken all chips%
   lvl = graythresh(B2);
   C = im2bw(B2,lvl); %Convert to black & white
   D = imcomplement(C); %Obtain negative%
   E = bwmorph(D,'clean'); %Remove noise%
   F = imdilate(E,Se); %Thicken chips%
   CC = bwconncomp(I,8); %Obtain count%
   %Plot of chips vs frame number%
   plot(time,CC.NumObjects,'-o');
```

```
    hold on
    a=0;
    i=i+1;
    flushdata(vid); %Clear memory%
    toc
end
stop(vid) %Close video%
fclose(SerPSoC) %Stop communication%
delete(SerPSoC) %Delete communication port%
clear SerPSoC
```

APPENDIX D

ANOVA ROBUSTNESS TEST FOR FIRST TYPE-1 TEST

The following are the ANOVA robustness test plots for the first type-1 test

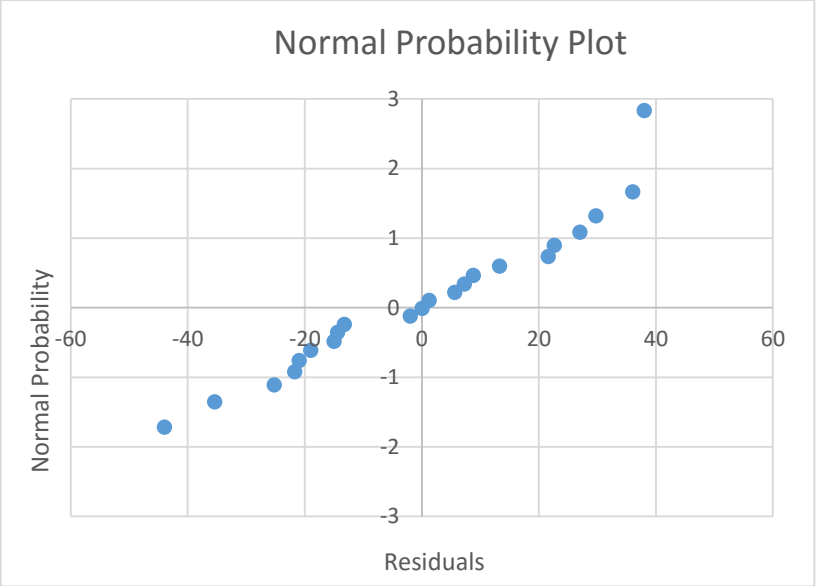

Barring a single outlier, the residuals follow a normal distribution. This is seen by a simple ‘fat-pencil’ test.

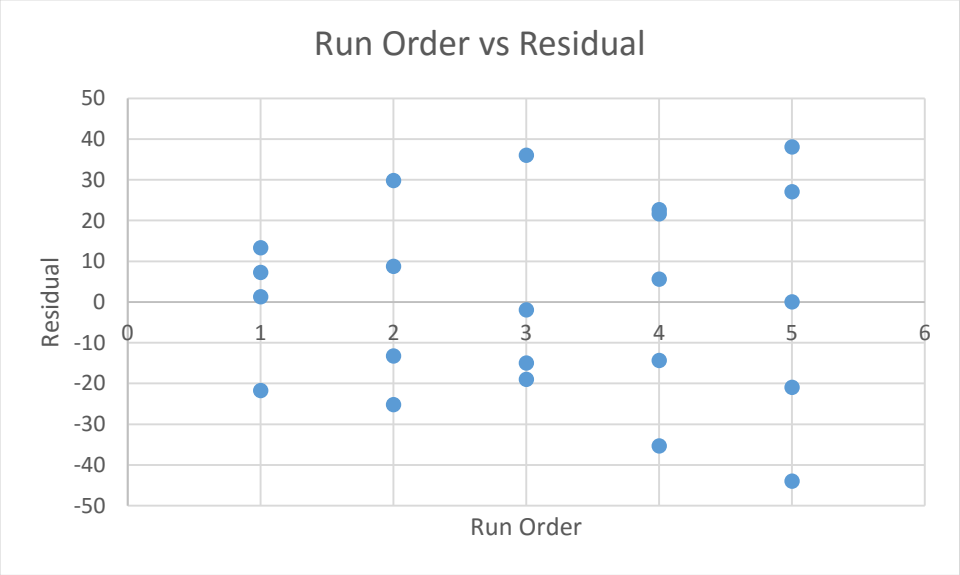

APPENDIX E

ANOVA ROBUSTNESS TEST FOR FIRST TYPE-1 TEST

The following are the ANOVA robustness test plots for the second type-1 test

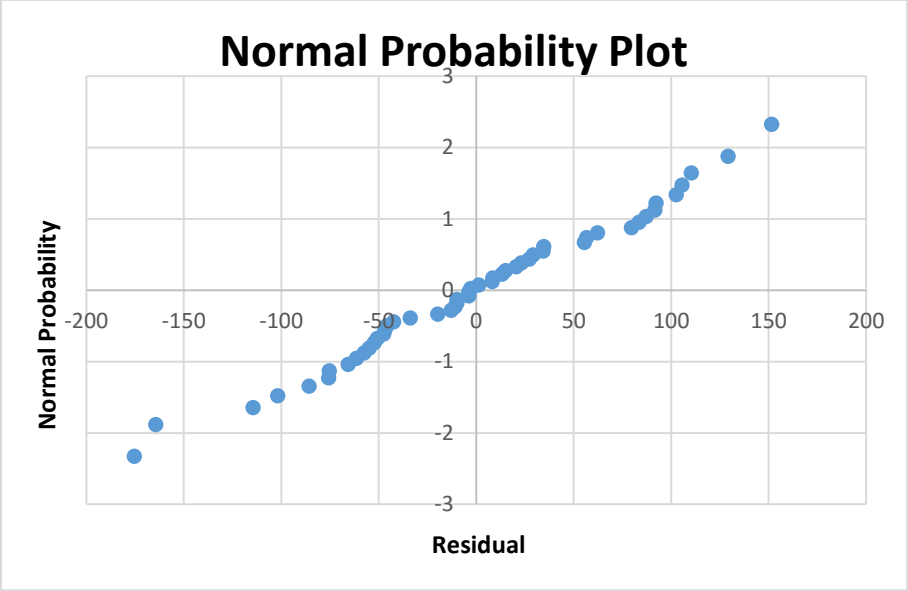

The normal Probability plot shows that the residuals exhibit a normal distribution. The Figure below shows the plot of residuals vs run order. The run order plot reveals that there is a correlation between residual and run-order. This is expected, as the random experiment order was such that the lower feedrates were performed later. The variance has been observed to be lower for the slower feedrates, where chip count was found to be lower; meaning that the variance is acting as a percentage of the mean.